Crustal Structure and Stratigraphy of the South Mozambique Margin to South Mozambique Ridge From Combined Wide-Angle and Reflection Seismic and Drill Hole Data

Philippe Schnürle, A. Leprêtre, Mikael Evain, Fanny Verrier, P. De-clarens, Joseph Thompson, N. Dias, A. Afilhado, A. Loureiro, Sylvie Leroy, et al.

AGU ADVANCING EARTH AND SPACE SCIENCE

Earth and Space Science

RESEARCH ARTICLE
10.1029/2021EA001902

Crustal Structure and Stratigraphy of the South Mozambique Margin to South Mozambique Ridge From Combined Wide-Angle and Reflection Seismic and Drill Hole Data

P. Schnürle[1], A. Leprêtre[1], M. Evain[1], F. Verrier[1], P. De-Clarens[2], Joseph Thompson[1], N. Dias[3], A. Afilhado[3], A. Loureiro[3,4], S. Leroy[5], E. d'Acremont[5], D. Aslanian[1], and M. Moulin[1]

[1]Geo-Ocean, CNRS, Ifremer, UMR 6538, University of Brest, Plouzane, France, [2]TOTAL, R&D, Pau, France, [3]IDL—Instituto Dom Luiz (IDL), Faculdade de Ciências, Universidade de Lisboa, Lisboa, Portugal, [4]ISEL—Instituto Superior de Engenharia de Lisboa, Lisboa, Portugal, [5]CNRS-INSU, Institut des Sciences de la Terre Paris, ISTeP UMR 7193, Sorbonne Université, Paris, France

Abstract We have analyzed the MZ6 onshore-offshore wide-angle seismic profile of the MOZ3-5 survey to investigate the crustal structure of the South Mozambique passive margin. The NNW-SSE, 625 km-long profile runs across the Mozambique coastal plain (MCP), the Continental Shelf and Slope, the Almirante Leite Ridge (ALR), the North Natal Valley (NNV), the Ariel Graben and the Dana Plateau of the Mozambique Ridge. Forward modeling through combined interpretation of the multichannel seismic, the main reflected and refracted phases of the wide-angle, drill hole data and bathymetric data reveal: (a) a sedimentary cover poorly compacted up to 3 km-thick, intruded by magmatic dykes that reach the seafloor at the ALR forming 0.5 to 5 km-wide corrugated mounts, (b) between 2 and 7 km, thick magmatic or volcano-clastic deposits are observed both at the MCP and NNV, forming a 40 km-wide terrace at the center of MZ6 and southward-dipping reflectors in the southern part interpreted as the Pre-Neocomian Formation contemporary of the Karroo and/or Bombeni-Movene magmatic events reached in several wells, (c) onshore, the 3-layered crust reaches 39 km thickness, gradually thinning to ~27 km at the southern end of MZ6. In the deepest layer, velocities exceed 7.15 km/s, reaching at its base 7.55 km/s at the vertical of the ALR. (d) the seismic Moho is marked by a strong reflection on the wide-angle data. These results suggests that the basement is composed of slightly thinned and altered continental crust, most likely intruded by several phases of intense magmatism.

Plain Language Summary About 200 Ma ago, the mega-continent Pangaea broke up. The dispersion of the pieces, linked to the closure and disappearance of the Thetys paleo-ocean, gave the birth of the Atlantic and Indian Oceans. In detail, the initial position of each piece of this jigsaw is of great importance as it has an impact on our understanding of the genesis of the continental passive margins, the role of tectonic inheritance, the pre-rift and post-rift evolution of the topography dynamic (vertical movement) and of the geodynamic of the plates (horizontal movement). Nevertheless, in the Western Indian Ocean, the initial pre-beak-up position of Antarctica plate respect to Africa plate is still under debate, mainly due to the lack of deep geophysical data. In 2016, an academic-industrial collaboration succeeded in acquiring deep information along seven seismic profiles crossing the North Natal Valley (NNV) off the coast of Mozambique. The results falsify the presence of an oceanic crust in that area and thus most of the plate reconstruction models. The NNV presents a thick continental crust intrudedded by several phases of intense magmatism, with at its top, a volcano-clastic pre-Neocomian Fm contemporary of the crustal thinning and subsequent spreading between Africa and Patagonia plates.

Key Points:

- The North Natal Valley (NNV) presents a ~30 km-thick continental crust, in contrary to what is proposed in most geodynamic models
- Velocity variations in the middle-lower part of this crust probably represent mantle intrusions during several phases of intense magmatism
- On the top of the basement, there is a volcano-clastic pre-Neocomian Fm, probably contemporary of the movement of the Patagonia plate

Supporting Information:

Supporting Information may be found in the online version of this article.

Correspondence to:

P. Schnürle,
philippe.schnurle@ifremer.fr

Citation:

Schnürle, P., Leprêtre, A., Evain, M., Verrier, F., De-Clarens, P., Thompson, J., et al. (2023). Crustal structure and stratigraphy of the South Mozambique Margin to South Mozambique Ridge from combined wide-angle and reflection seismic and drill hole data. *Earth and Space Science*, *10*, e2021EA001902. https://doi.org/10.1029/2021EA001902

Received 2 OCT 2021
Accepted 24 MAR 2023

Author Contributions:

Conceptualization: D. Aslanian, M. Moulin
Formal analysis: P. Schnürle, A. Leprêtre, M. Evain, F. Verrier, S. Leroy, E. d'Acremont

1. Introduction

Located in the south-east corner of Southern Africa, the Southern Mozambique Basin is an area flanked on the west and the north-west by pre-Palaeozoic structures: the Kaapvaal and the Zimbabwe Cratons, respectively. The external limits of this basin are defined by the succession of the north–south Lebombo monocline and the north-east to south-west Mwenetzi monocline. The Natal Valley and Mozambique Ridge (MozR) of South Africa are considered to have formed as the result of separation between the South America-Africa-Madagascar and Antarctic continents (e.g., Tikku et al., 2002). The crustal structure of these passive margins has been the subject of debate, as well the transition between the strike-slip margin related to the (Oxfordian) Africa-Antarctica breakup

Investigation: M. Evain, N. Dias, A. Afilhado, A. Loureiro, D. Aslanian, M. Moulin
Methodology: P. Schnürle, A. Leprêtre, M. Evain, P. De-Clarens, Joseph Thompson, D. Aslanian, M. Moulin
Project Administration: M. Evain, D. Aslanian, M. Moulin
Supervision: P. Schnürle, M. Evain, D. Aslanian, M. Moulin
Visualization: P. Schnürle, M. Evain, F. Verrier, P. De-Clarens, Joseph Thompson, D. Aslanian, M. Moulin
Writing – original draft: P. Schnürle, F. Verrier, D. Aslanian
Writing – review & editing: P. Schnürle, M. Evain, D. Aslanian, M. Moulin

(East Limpopo) and the pull-apart divergent margin related to the Africa-South America breakup (North Natal) when the withdrawal of the Falkland-Malvinas Plateau was accommodated by Valanginian dextral strike-slip movement along the Agulhas-Falkland Fracture Zone (e.g., Mueller & Jokat, 2019; Thompson et al., 2019). As such, the crust underlying the northern Natal Valley, immediately to the north of the active Agulhas transform margin, could represent a divergent or "pull-apart'' passive margin, linking the Agulhas transform margin and the transform margin of Eastern Mozambique, however its tectonic history is not well known and most of the recent kinematic-models present the Mozambique coastal plain (MCP) and the North Natal Valley (NNV) as an oceanic crust overlain by LIP-type magmatic event (see Thompson et al., 2019 for a review). In addition to trans-tensional tectonics, the crust has been affected by episodes of uplift (e.g., Baby, 2017), oceanic flood basalt outpouring associated with emplacement of the Mozambique aseismic Ridge (MozR, e.g., Ben-Avraham et al., 1995; Fischer et al., 2017; Gohl et al., 2011; Jacques et al., 2019), and subsidence relating to cooling of the margin and sedimentary loading (e.g., Leprêtre et al., 2021; Moulin et al., 2020).

To better evaluate the tectonic history of the South Mozambique Margin, we investigate its crustal structure with geophysical data acquired during the MOZ3-5 survey (2016). During the MOZ3-5 survey (2016) of the integrated multidisciplinary PAMELA (PAssive Margin Exploration LAboratory) project conducted by TOTAL, IFREMER, in collaboration with French Universities, CNRS and IFPEN, new geophysical and geological data were acquired (bathymetry, piston cores, water column, sub-bottom profiler, gravity, magnetism, dredges, wide angle and reflection seismic) with 193 deployments of Ocean Bottom Seismometers from the Ifremer's Marine Geosciences pool over seven wide-angle seismic (WAS) lines on the southern-Mozambique and Limpopo margin (Figure 1). Five profiles were extended onshore in the MCP with 124 landstations. The present article focuses on one of the main profiles, the profile MZ6, oriented NNW-SSE and 625 km in length, running across the MCP, the continental shelf and slope (CSS), the Almirante Leite ridge (ALR), the NNV, the Ariel Graben (AG) and the Dana Plateau of the MozR. Thanks to our collaboration with Total and Schlumberger, it also benefits Sunray1 drilling information that can be extended along a MCS industrial WesternGebco profile to MZ6 profile.

2. Data and Method

2.1. Profile Locations

MZ6 is a 625 km long on-shore off-shore wide-angle profile located in the NNV and orientated NNW-SSE. It spans from the MCP onshore (MCP), across the Mozambican CSS, the Central Terrace (CT) and the southern domains of the North Natal Valley (S-NNV), and ends at the very northern part of the MozR to the south. The MozR was partly defined by a continuous bathymetric and gravimetric feature (Figure 1). While its southern portion, southward of the AG, is characterized by intense magmatism (e.g., Fischer et al., 2017; Jacques et al., 2019), its northern portion, between 28 and 22°S, is formed by large contouritic units on thin continental-intermediate crust, as imaged along the MZ1, MZ4, and MZ5 profiles (Leprêtre et al., 2021; Moulin et al., 2020; Watremetz et al., 2021). Hence, in our paper, the MozR will represent the magmatic structure south of the AR, which is crossed by the MZ6 profile.

2.2. Wide-Angle Data Acquisition

At sea, a total of 25 Ocean Bottom Seismometers (OBS with four components: Hydrophone plus 3-Comp. Seismometer) were deployed, spaced every 7 nmi, between 0 and 300 km model distance in water depths of 112–1,690 m. Inland, the profile was extended 100 km toward the North-North-West with the deployment of 21 Land Seismic Stations (LSS- Reftek 125A-01 and L-4C, spaced every 5 km). The source was composed of an array of 15 airguns, synchronized on the first peak and providing a total volume of 6,500-in^3, with shot interval every 60 s. The 2,974 air-gun shots along MZ6 start slightly south of MZ6OBS01 (296 km model distance) extending 185 km south of MZ6OBS25 and were recorded by all instruments and a marine 720-channel streamer 4.5 km in length. This profile runs parallel to the MZ7 profile (Leprêtre et al., 2021) about 80 km eastward and crosses the MZ1, MZ2, and MZ3 (Evain et al., 2021) profiles at the positions of the MZ6OBS18, MZ6OBS08, and MZ6OBS15, respectively. It presents therefore three crossing points that constrain our model.

2.3. Seismic Data Processing and Modeling

Ifremer's SolidQC software was used for pre-processing the multi-channel seismic data (MCS), performing data quality control and signal-to-noise ratio, 2D geometry and binning, and SEG-Y file generation. Then, this

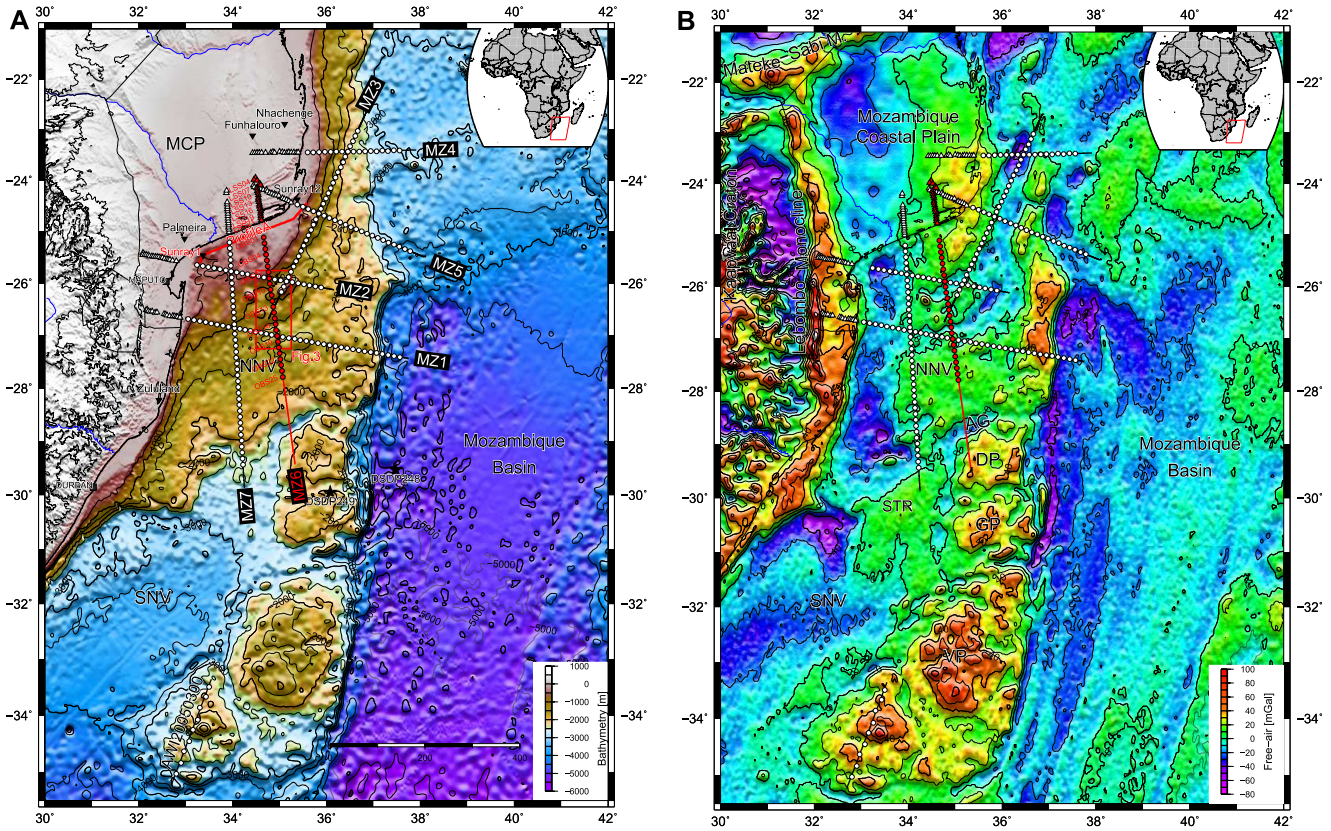

Figure 1. Location map of the MOZ3-5 survey. (a) The topography (ETOPO1) is shaded from the North. The MZ6 profile is indicated in red, remaining wide-angle seismic (WAS) profiles in white. OBS are marked by circles, LSS by triangles. AWI2005030 WAS profile is indicated in black. Profile A reference reflection profile is indicated by a red line. Petroleum boreholes are indicated by black inverted triangles. DSDP sites 248 and 249 are marked by black stars. A red square delimits the 3D view of Figure 3. MCP: Mozambique Coastal Plain; NNV: North Natal Valley; SNV; South Natal Vall. (b) Free-air gravity anomaly (Sandwell & Smith, 2009). NNV, North Natal Valley; SNV, South Natal Valley; STR, South Tugela Ridge; AG, Ariel Graben; DP, Dana Plateau; GP, Galathea Plateau; VP, Vauban Plateau.

streamer seismic data were processed with the Geocluster (CGG-Veritas) software for spherical divergence corrections, wave equation multiple attenuation, shot-gather predictive deconvolution, time variant band-pass filter, and radon transform multiple attenuation. Finally, dip-move-out followed by water-velocity FK migration as well as pre-stack Kirchhoff time migration (PSTM) were performed.

In order to verify the accuracy of the wide-angle velocity model, the MCS data is pre-stack depth migrated and residual move-out analysis is performed. The Pre-stack Depth Migration (PSDM) processing is performed with the Seismic Unix package (Cohen & Stockwell, 2003; Stockwell, 1999). The PSDM consists in two steps: ray tracing and seismic data depth migration. First, travel-time tables regularly spaced at 150 m along the profile are computed by paraxial ray tracing on a 50 m × 25 m spaced grid, while travel-times in shadow zones are compensated by solving the eikonal equation. Second, common offset Kirchhoff depth migration is performed: migrated traces are output as common image gathers (CIG) binned at 25 m with 30 offset-classes between 290 and 4,640 m spacing at 150 m. Dip-independent velocity analysis can then be performed on the migrated CIG by analyzing residual move-out. Hence, if the velocity model used for migration is close to the true medium velocity, all common offset migrated panels map the recorded seismic events to the same reflector depth, else the move-out from near to far offset translates into an interval velocity correction (Liu & Bleistein, 1995). Moreover, depth migrated gathers are excellent records of amplitude variations with offset, and therefore are indicators of in-situ rheological changes. The residual move-out behavior together with the seismic character from PSDM images are key elements to locate accurately major geological contacts, moreover with higher horizontal resolution when compared to the OBS records.

Pre-processing of the OBS data included internal clock-drift correction to the GPS base time, band-pass filter, and relocation of the instrument using the direct water wave. Then upward and downward traveling waves were separated (Schneider & Backus, 1964) by combining hydrophone and vertical OBS components. Spiking predic-

tive deconvolution was applied to the upward traveling record designed on the downward traveling wave. Traces were scaled with a gain proportional to the offset in order to enhance the refracted events. The data from LSSs composing an array were first debiased and band-pass filtered, and the array was stacked. The aim of forward modeling is to produce a layer-based (structural) P-wave velocity model that best fits the travel-times (within their uncertainty range) and amplitudes of the observed seismic events reflected at each interface and refracted between interfaces (Zelt, 1999; Zelt & Barton, 1998). We utilize the Rayinvr package (Zelt & Smith, 1992) to perform the joint wide-angle data and MCS section, following a layer-stripping strategy, and iterative damped least squares travel-time inversion at later stages. Interfaces were selected at travel-times where clear and strong amplitude events are observed and a major velocity change occur. The initial interval velocity was guided by the converted RMS velocity of the MCS pre-stack gathers and NMO analysis of the OBS gathers.

3. Results

3.1. Seismic Reflection Data

The PSTM MZ6MCS section (Figure 2) can be subdivided into the CSS (between 207 and 295 km model-distance) formed by the Limpopo alluvial cone (Km 220 on Figures 2 and 3), the Amirante Leite Ridge (ALR, between 105 and 207 km), a prominent basement high: the CT (between 70 and 105 km), the southern North Natal Valley (S-NNV, between −118 and 70 km) and the MozR (between −190 and −118 km). The quality of the MZ6MCS seismic reflection data is generally good, but its penetration is poor.

3.1.1. Continental Shelf and Slope

Along the shelf and slope of MZ6MCS profile (Figures 1 and 3), a sequence of relatively continuous and generally conformable reflectors, characterized by relatively week amplitude, about 1 s twt in thickness, are imaged beneath the seafloor (S1–S3). Underneath, high amplitude gently undulating reflections are observed: this sequence (S4), between 50 and 150 ms twt thick, is convex in shape reaching its largest burial depth at 2.3 s twt near 220 km model distance. The base of this sequence is difficult to trace but coincides with a general loss of seismic penetration, signal scatter and poorly continuous events (SV2); However between 220 and 250 km model distance, southward dipping reflections are imaged between 2 and 3 s twt, with a dip increasing both with depth and southward.

3.1.2. Amirante Leite Ridge

A series of highs mark the foot of the continental slope, culminating at 300 m water depth along the MZ3 profile (Figure 3) from the sedimentary cover, producing a rough seafloor easily identifiable on bathymetric data. Along the MZ6MCS profile between 160 and 200 km model distance, the rough bathymetry produces seismic scatter at the seafloor (Figure 2). Underneath, the sequence of relatively continuous reflectors observed in the Limpopo Cone extends southward (S1–S3), about 1 s twt thick, until 105 km model distance where it is truncated against the CT. While this sequence is interrupted below the most prominent topographic mounts, it is only poorly disturbed below the smaller mounts. At about 1.75 s twt, a thin (up to 0.25 s twt) sequence (SV1) of high-amplitude reflections is observed, between the light green and the dark green horizon on Figure 2. It rests on top of a 0.75 s twt thick unit (SV2), characterized by an undulating top, fairly discontinuous internal bedding, and a relatively abrupt loss of seismic penetration at its base.

3.1.3. Central Terrace

Between 75 and 110 km model distance, a wide basement high, mostly devoid of sedimentary cover, is imaged. On the bathymetric data, the basement high is identifiable as a broad mount of about 20 km in diameter around the MZ1-MZ6 crossing. The seafloor presents however much less roughness when compared to the ALR. On either sides of CT, the stratigraphy is very similar from S1 to SV2. On the southern flank, S1–S3 units are truncated, while SV1 drapes the basement high.

3.1.4. Southern North Natal Valley

Between 70 and −118 km model distance, from the CT to the AG, the seafloor progressively deepens from 2 to 4 s twt, while the stratigraphic units thicken. Beneath the highly reflective S3, the undulating unit SV1 preserved its 0.75 s twt thickness and retains its discontinuous wavy seismic character, while deepening from 2.5 s twt (25 km) to 5.4 s twt (−100 km). Its strata presents areas of increasing southward dip bounded by sub-vertical normal faults at the northern shoulder of basement highs, in a pattern of ∼40 km wide horst and graben. Its base

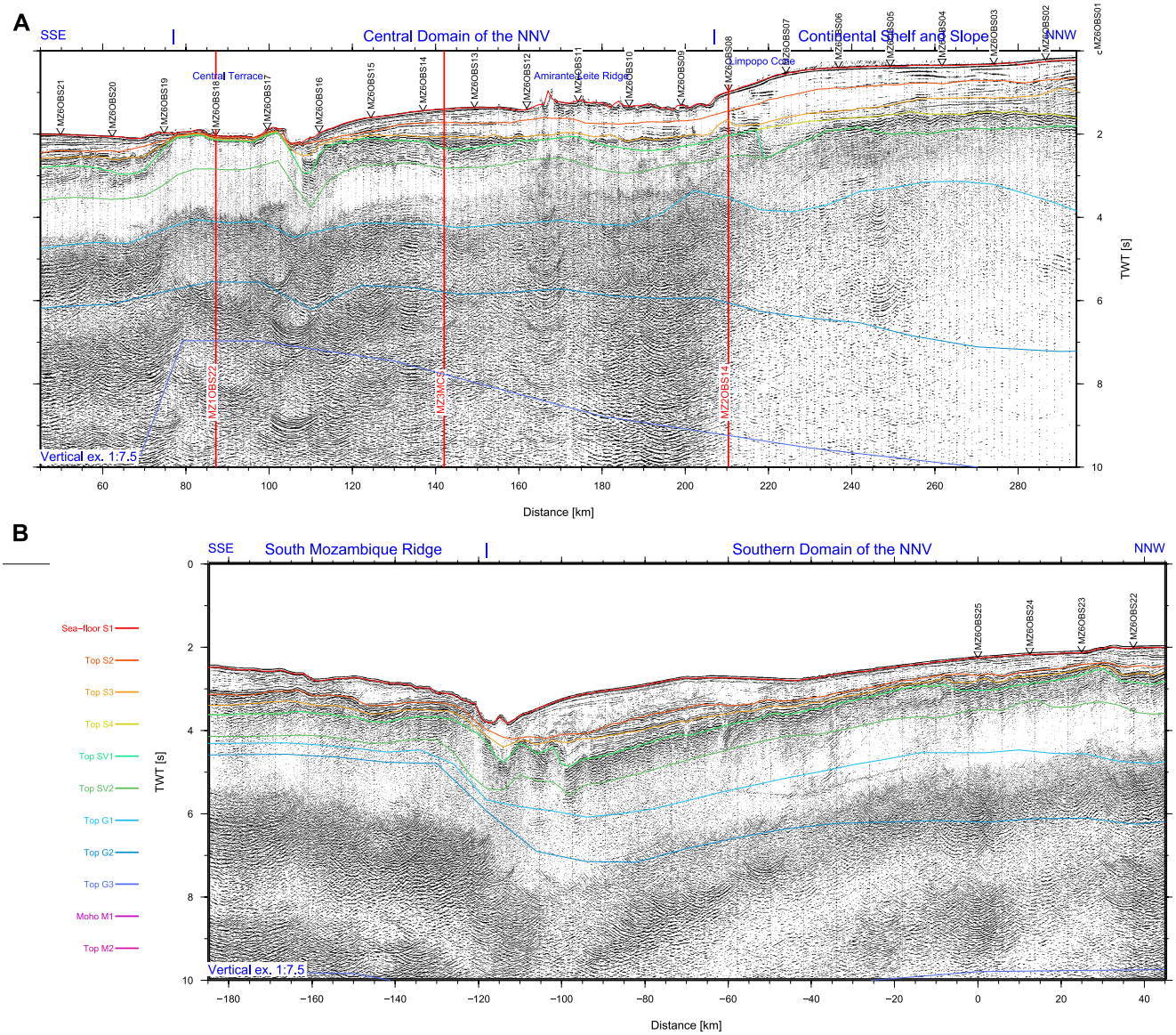

Figure 2. Two-way travel-time record section of MCS data along MZ6 profile overlain by time converted interfaces of wide-angle model. (a) Northern part; (b) Southern part; The intersections with the MOZ3-5 data set are indicated by red line. OBS location are indicated by white triangle. Vertical exaggeration at seafloor is 1:7.5.

(SV2) remains difficult to trace as the seismic penetration drops more continuously with depth, and several southward dipping events cross locally SV2. At the bottom of the Southern NNV, an erosive channel, the AG, runs in a WSW-ENE direction along the northern flank of the MozR (Figures 1 and 3).

3.1.5. South Mozambique Ridge

This AG erosive channel truncates most of the strata overlying SV1, revealing a sharp rise (~1.5 s twt) of the basement along two horst and graben systems (between −15 and −185 km model distance) presenting a similar seismic character to the S-NNV. The southward dipping SV1 strata are top-laped unconformably by the high amplitude S3 and nearly transparent S1 sequence about 0.75 s twt thick (Figure 2).

3.2. Forward Modeling

From receiver records (OBS and LSS), the full subsurface sedimentary, crustal, and mantle sequence is imaged to offsets reaching 120–230 km. Ps1 to Ps4 refracted arrivals, traveling with apparent velocity increasing from 1.7 km/s (close to the water-cone) to 2.55 km/s (locally 3 km/s), are observed as secondary arrivals (represented

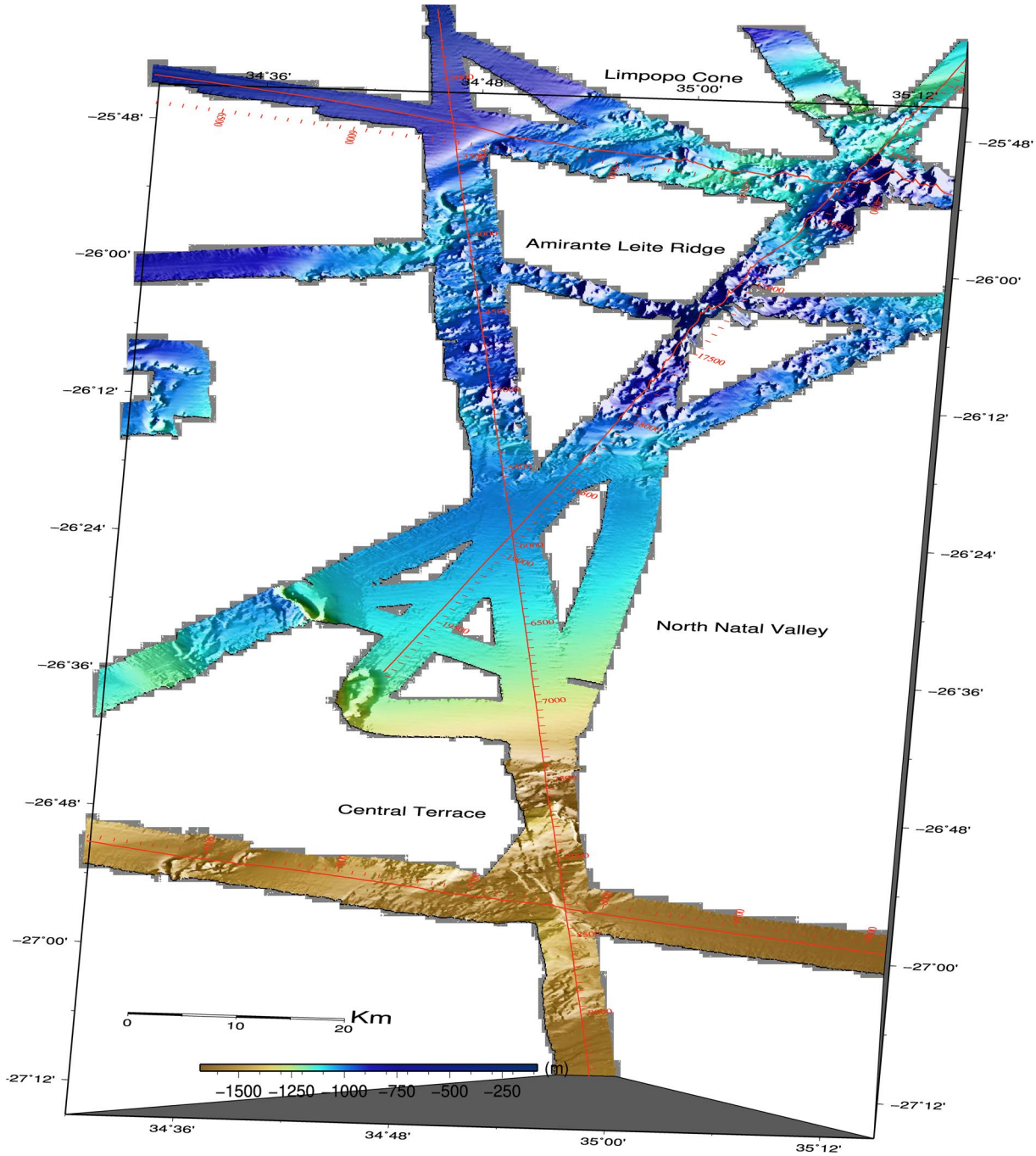

Figure 3. Bathymetric shaded 3D view of the Amirante Leite and Central Terrace. The high resolution swath-bathymetric data is shaded from the SSE. The location of the MOZ3-5 MCS profiles are draped in red and annotated in CMP.

with red, orange, yellow; Figure 4A). However on MZ6OBS20 (Figure 4B) and MZ6OBS21, short lived (<5 km offset) 5 km/s apparent velocity refractions occur within S2 and S3 that coincide with bright reflections on the MZ6MCS profile. The SV1 layer replaces the S4 layer south of 217 km model distance and presents a strong gradient with an increase of the top velocity from 3.4 km/s at 170–4.25 km/s at 200 km (but decreasing to 3.8 at 215 km, the northern tip of SV1) and bottom velocity of 4.85 km/s (decreasing to 4.3 at 215 km). Furthermore, a 150 ms travel-time gap separates the refracted Psv1 and Psv2 on MZ6OBS14 (Figure 4C) to MZ6OBS16 indicating that the velocity in SV1 layer is very -heterogeneous with fast (~5 km/s) and slow interbeds. Psv2 generally appears as first arrival (light green and olive) with a velocity increasing from 4.85 to 5.0 to 5.9–6.3 km/s.

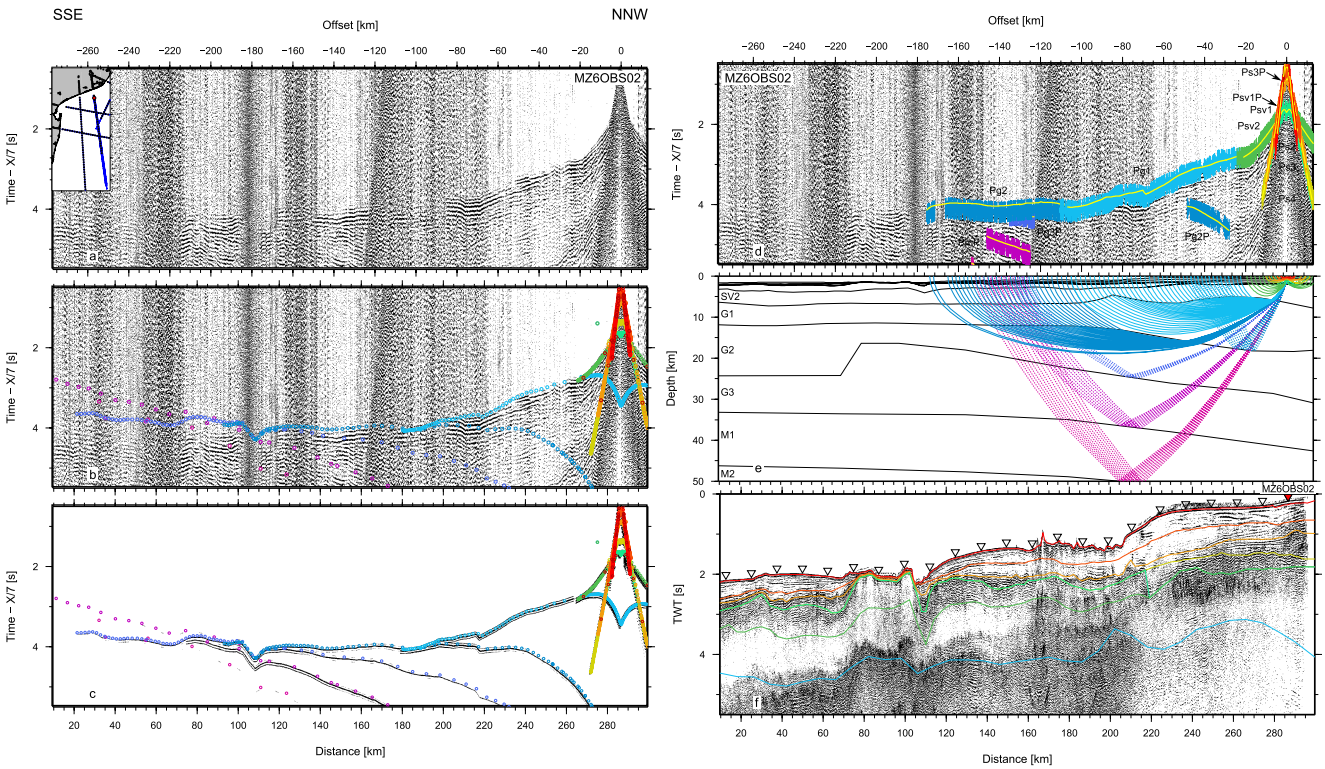

Figure 4. (A) MZ6OBS02. (a) Seismic record; (b) Seismic record overlain by predicted times (circle); (c) Color coded synthetic; (d) Observed travel-times (bar) overlain by predicted time (yellow line); (e) Seismic rays; (f) MCS time migrated section and color-coded model interfaces. On (a–d), travel-time is reduced by a velocity of 7 km/s. (B) MZ6OBS20. (a) Seismic record; (b) Seismic record overlain by predicted times (circle); (c) Color coded synthetic; (d) Observed travel-times (bar) overlain by predicted time (yellow line); (e) Seismic rays; (f) MCS time migrated section and color-coded model interfaces. On (a–d), travel-time is reduced by a velocity of 7 km/s. (C) MZ6OBS14. (a) Seismic record; (b) Seismic record overlain by predicted times (circle); (c) Color coded synthetic; (d) Observed travel-times (bar) overlain by predicted time (yellow line); (e) Seismic rays; (f) MCS time migrated section and color-coded model interfaces. On (a–d), travel-time is reduced by a velocity of 7 km/s. (D) MZ6OBS25. (a) Seismic record; (b) Seismic record overlain by predicted times (circle); (c) Color coded synthetic; (d) Observed travel-times (bar) overlain by predicted time (yellow line); (e) Seismic rays; (f) MCS time migrated section and color-coded model interfaces. On (a–d), travel-time is reduced by a velocity of 7 km/s. (E) MZ6LSS21. (a) Seismic record; (b) Seismic record overlain by predicted times (circle); (c) Color coded synthetic; (d) Observed travel-times (bar) overlain by predicted time (yellow line); (e) Seismic rays. On (a–d), travel-time is reduced by a velocity of 8 km/s. (F) MZ6LSS02. (a) Seismic record; (b) Seismic record overlain by predicted times (circle); (c) Color coded synthetic; (d) Observed travel-times (bar) overlain by predicted time (yellow line); (e) Seismic rays. On (a–d), travel-time is reduced by a velocity of 8 km/s.

The crustal Pg1, Pg2, and Pg3 refracted phases (represented with cyan, light blue, and dark blue) form a relatively continuous event in both amplitude and apparent velocity, without sharp inflections indicative of major velocity changes between layers. First arrivals from shots fired north of the CT are clearly identifiable as crustal P1g traveling at 6.35–6.8 km/s, and P2g traveling at 6.90–7.1 km/s (Figures 4A and 4C). The G2 low velocity gradient prevents the seismic rays from turning at depth greater than 20 km even at 180 km offset. The southern most deployed MZ6OBS25 (Figure 4D) illuminates the upper crust G1 of the NNV and middle G2 and lower crust G3 as well as the upper mantle (PmP and Pm2P) of the CT. Pn refracted phases from the upper mantle (represented with magenta) are scarcely observed. Furthermore at near-critical incidence, weak-amplitude reflections are observed from the tops of the middle crust P2gP, lower crust Pg3P, and Moho PmP, from 60 to 160 km offset. Since no OBSs were deployed in the southern quarter of the profile between −184 and 0 km model distance, our model remains accurate only when the two-way time of each interface is accurately predicted by the MZ6MCS. As a matter of fact, records from MZ6OBS23 to MZ6OBS25 fits well the P1g, P2g, P3g, PmP, and PnP arrivals in the case where velocity in all layers remain constant south of MZ6OBS25.

The LSS installed onshore in the MCP present good quality data, with clear upper/middle/lower crustal refractions within 60–280 km offset, bright PmP reflection at the Moho, and a relatively clear Pn refracted in the upper-mantle to offsets reaching 360 km. Given that no shots were fired onshore, the LSS installed the closest to the shoreline (MZ6LSS21—Figure 4E to MZ6LSS19), while relatively noisy, are critical to estimate thickness variations of the upper layers in the MCP. Extending layers S2 to S4 at constant 2 km depth from 294 km

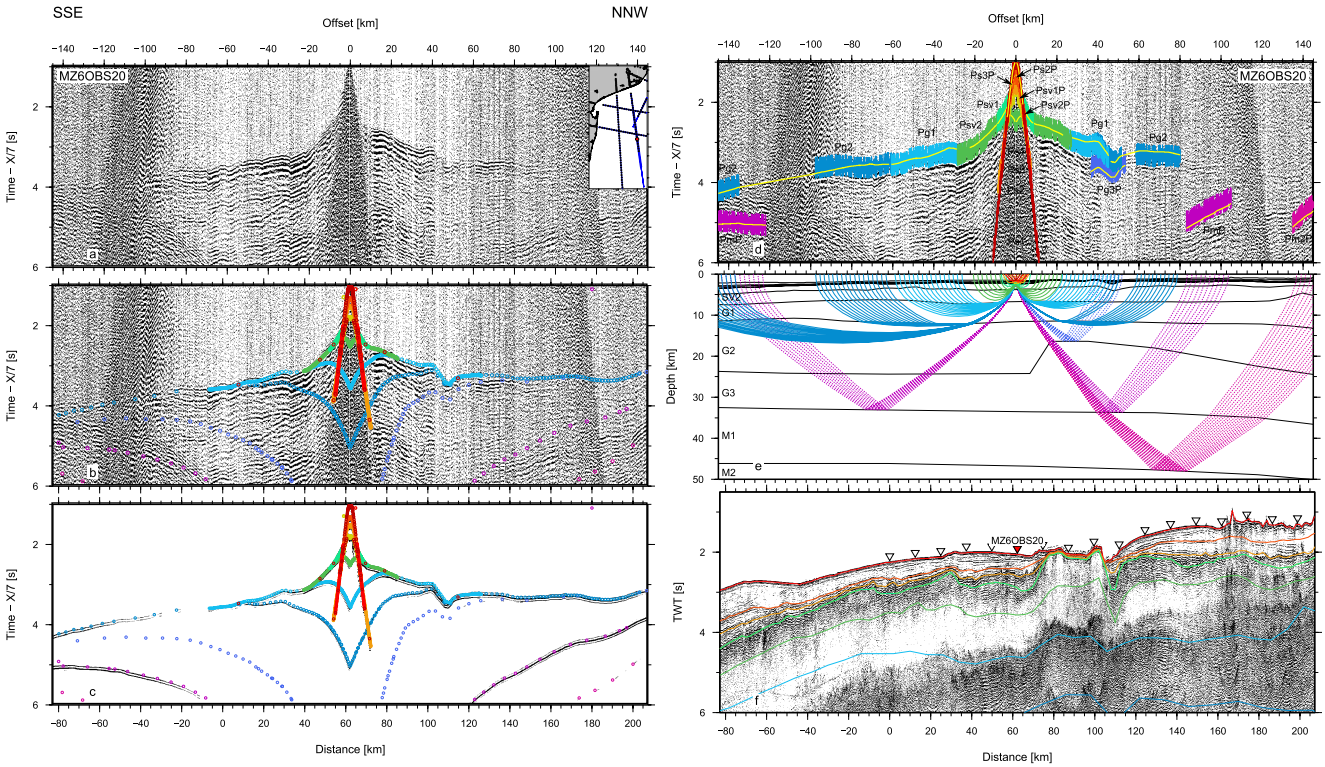

Figure 4. (Continued)

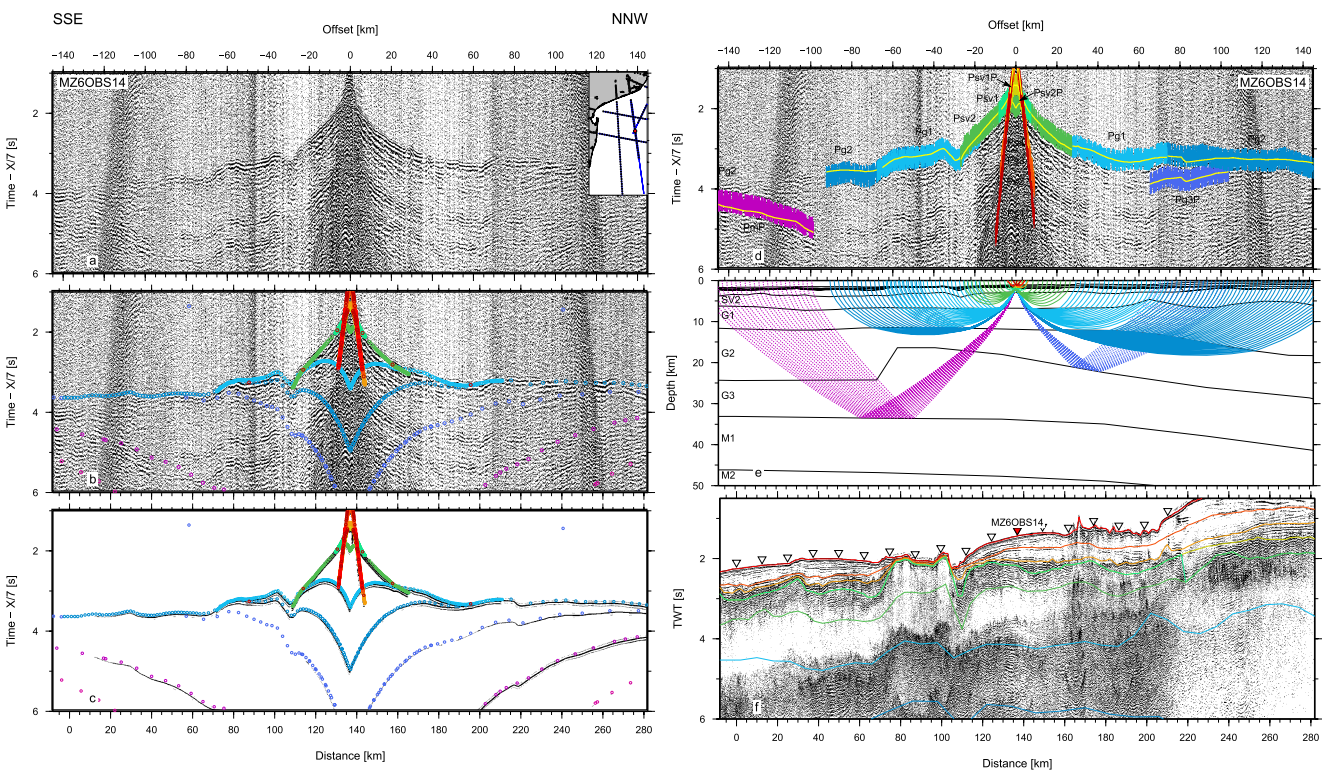

Figure 4. (Continued)

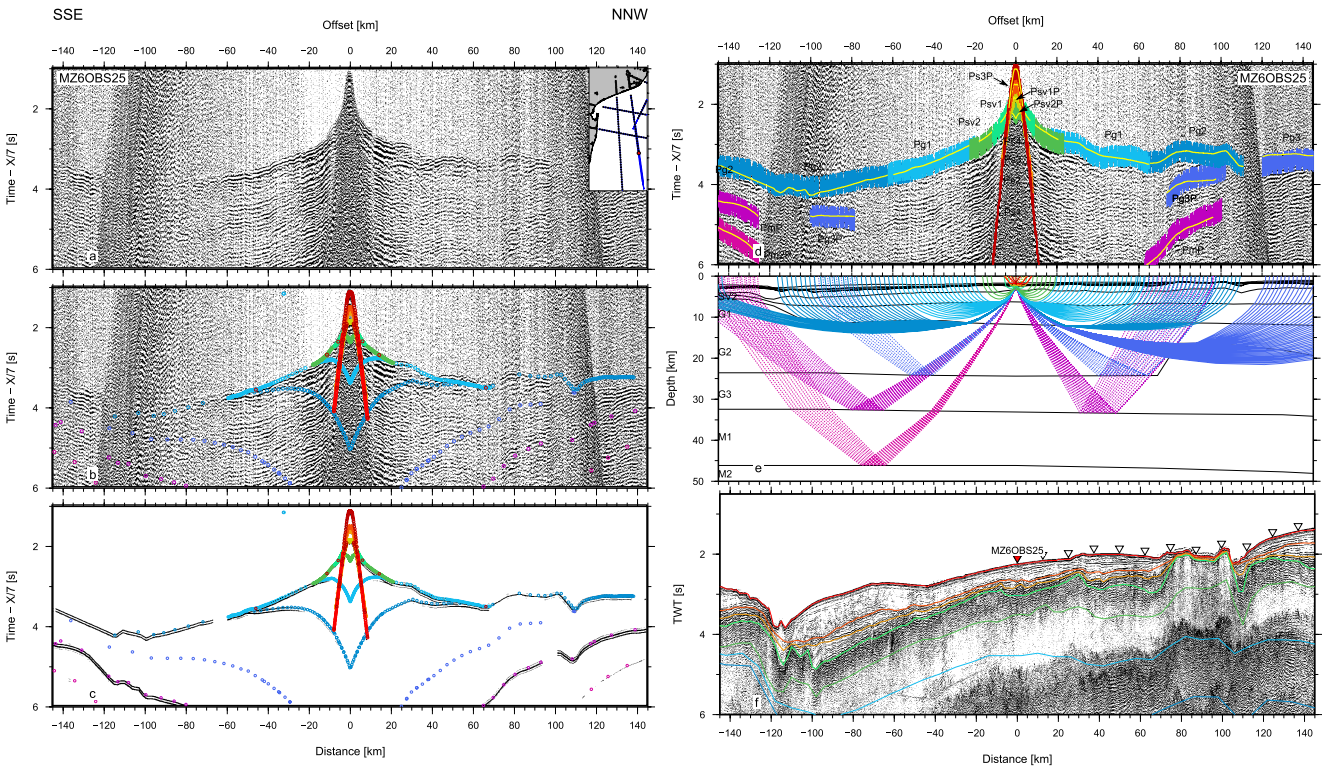

Figure 4. (Continued)

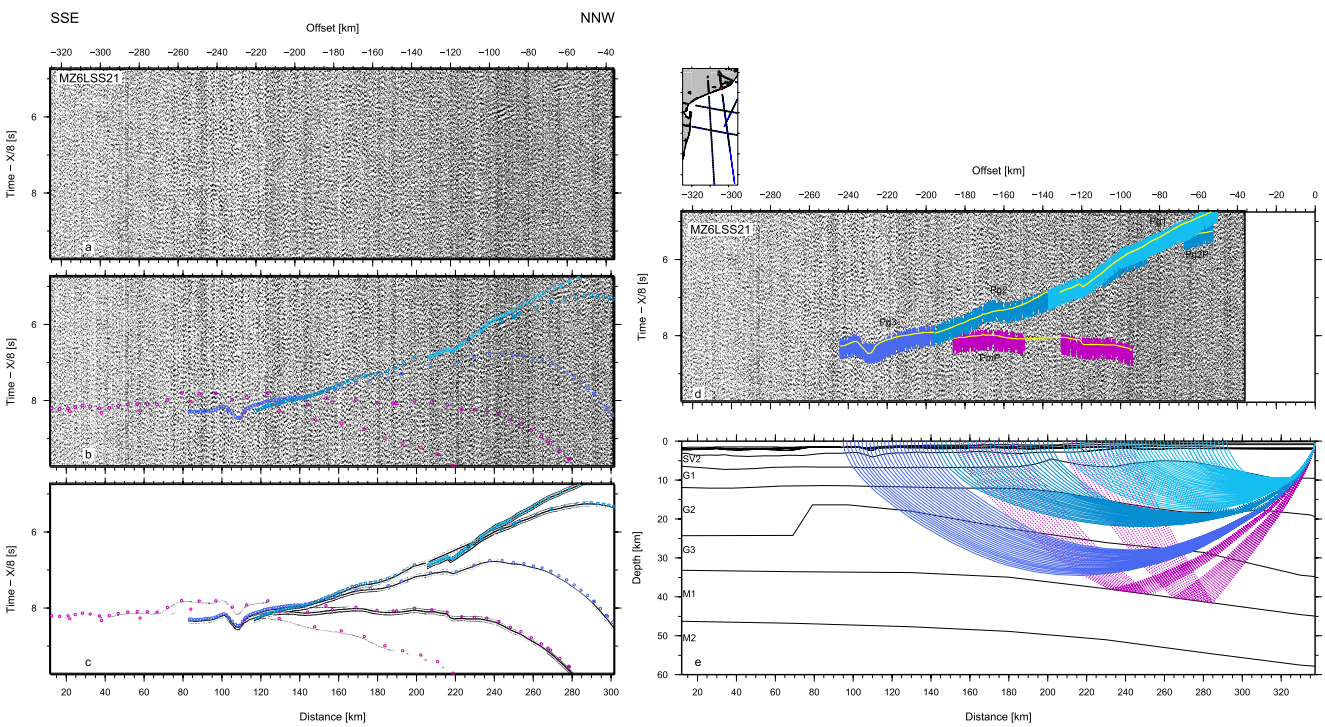

Figure 4. (Continued)

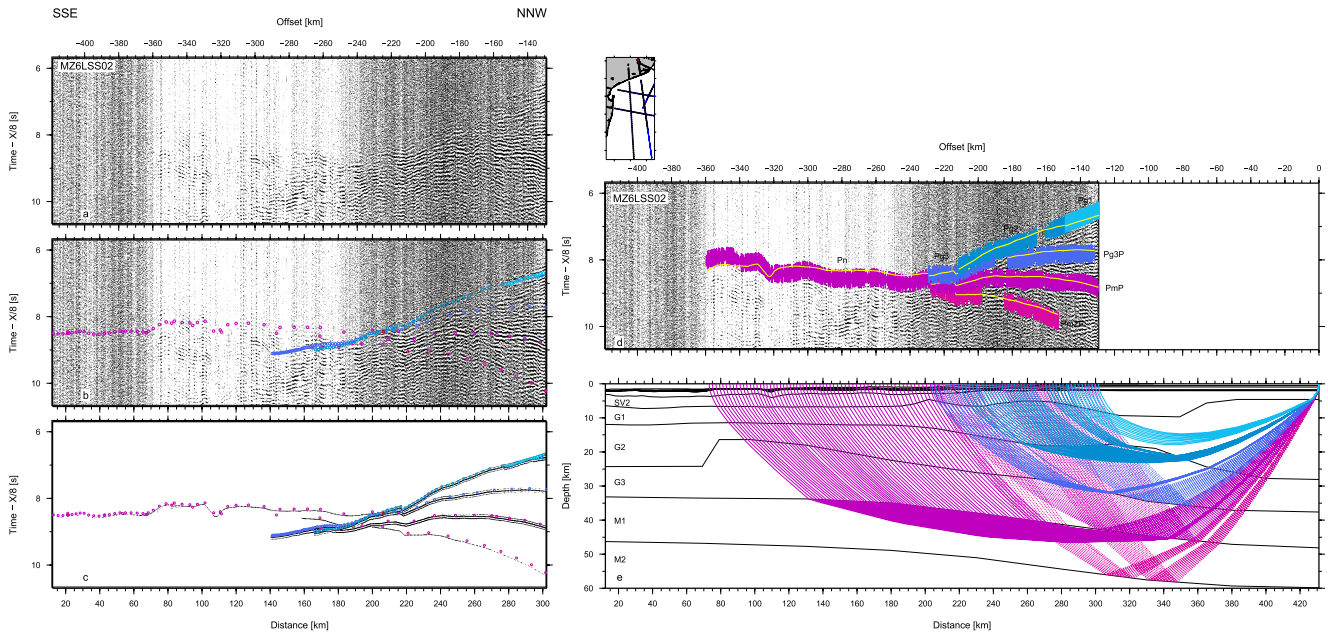

Figure 4. (Continued)

model distance to the norther extremity of our model, the G1 top deepens from 7 km at 280 km model distance to 10 km at 310–350 km model distance, then rises to 4.8 km depth between 350 and 383 km model distance, as observed from the earliest arrivals recorded by MZ6LSS16 to MZ6LSS11. The G2 top deepens from 18 km at 335 km model distance to 27 km at 400 km model distance. The Moho depth smoothly increases from 34 km at 150 km model distance to 47 km at 350 km model distance. The signal recorded by the LSS located northward further improves and illuminates the onshore portion of the crust and upper mantle (Figure 4E). As predicted by our synthetic records, the PmP becomes the brightest event (relatively), while the Pn gains in strength, traveling with an apparent velocity well above 8 km/s, and retains a butterfly wings shape observed on LSSs southward. This pattern is only partially due to the topography and sedimentary depression located at the transition between the ALR and the CT. The Pn arrivals display additional waviness and scatter that imply strong velocity variations when shots dive though the crust.

3.3. Travel-Time Inversion and Final P-Wave Velocity Model

From MZ6 wide-angle data, we digitized 113,085 events and interpreted their respective phases. Travel-time uncertainty was computed from the ratio of signal energy (in a 20 ms window) to average energy in the 68 ms preceding the signal according to Zelt and Forsyth (1994). The uncertainty ranges from 0.025 s for high ratio to 0.25 s for poor ratio. Our final velocity model is composed of four sedimentary layers S1 to S4, two mixed rheology layers SV1 and SV2, three crustal layers, and two mantelic layers and images their geometry to a depth of about 50 km (Figure 5). Tables 1 and 2 summarize reflected or refracted phase name, number of explained events, residual mean square, and normalized chi-square value, as well as instrument name, distance along model, direction code (−1 for rays traveling southward and 1 traveling northward), number of explained events, travel-time residual mean square, and normalized chi-square value, respectively The model explains the travel-time and phase of 106,119 events or 94% of total picks, with a global RMS travel-time residual of 0.09 s. Given our events individual (data driven) uncertainty, the model results in a normalized chi-square of 0.44. The average uncertainty is 0.193 s. The crustal and mantelic arrivals represent 52% and 31% of total events, respectively.

4. Model Evaluation

4.1. MCS Data Pre-Stack Depth Migration

Figure 6 presents the PSDM section, while CIG gathers extracted every 14 km along the profile and their associated semblance are in the supplementary data. While the sedimentary cover is imaged with great details, the

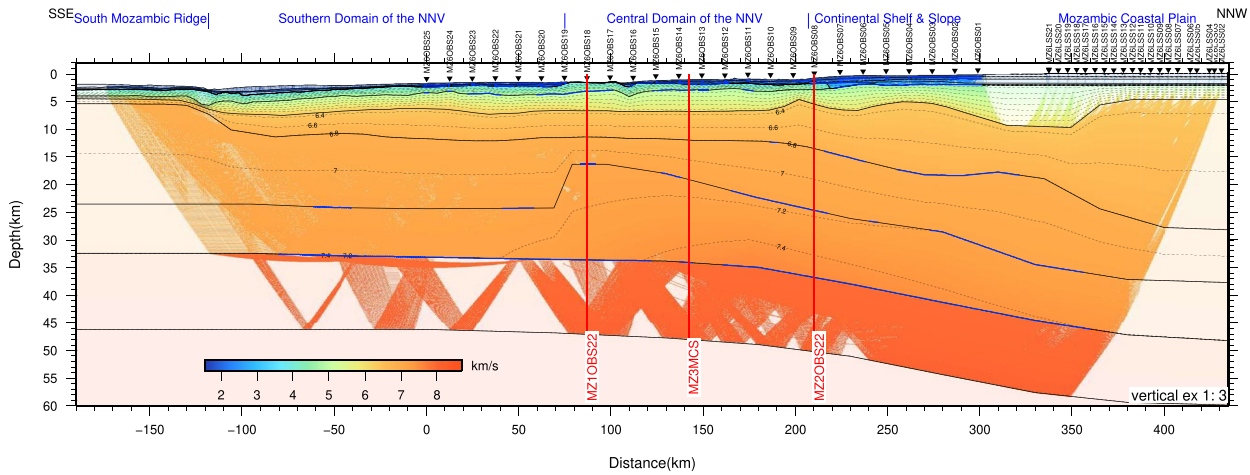

Figure 5. Final P-wave interval velocity model along MZ6 profile. Black lines mark model layer boundaries. Colored area are constrained by seismic rays. Inverted black triangle mark OBS positions. Blue lines mark the interfaces where reflection are observed on the wide angle records. Vertical exaggeration is 1:3.

semblance of the CIGs is poorly focused below the top of SV1 with sparse higher semblance events only observed in the NNV and MozR. In the CT and the ALR, the semblance is particularly blurred.

Table 1
Reflected or Refracted Phase Name, Number of Explained Events, Root Mean-Square Travel-Time Residual, and Normalized Chi-Square Value

Phase	Index	Npts	Trms (s)	Chi-square
Pw	1	1,619	0.098	0.564
Ps1	2	1,064	0.052	0.119
Ps2P	3	1,233	0.028	0.055
Ps2	4	667	0.046	0.147
Ps3P	5	243	0.024	0.045
Ps3	6	974	0.059	0.209
Ps4P	7	909	0.028	0.043
Ps4	8	161	0.046	0.147
Psv1P	9	726	0.023	0.045
Psv1	10	1,240	0.045	0.101
Psv2P	11	905	0.036	0.070
Psv2	12	4,964	0.057	0.212
Pg1P	13	0	X	X
Pg1	14	18,566	0.082	0.412
Pg2P	15	1,641	0.038	0.074
Pg2	16	26,370	0.098	0.543
Pg3P	17	4,470	0.053	0.160
Pg3	18	6,350	0.136	0.954
PmP	19	18,026	0.078	0.327
Pn	20	8,091	0.147	1.093
Pm2P	21	7,008	0.065	0.232

4.2. Indirect Model Evaluation

Models are evaluated not only by the number of justified observations and global data fit, but also by the model parametrization (node location; Figure 7a), the uniformity and density of their ray coverage, smearing, resolution and the number of rays that constrain each node (hitcounts; Figure 7b). Most interface and velocity nodes in our experiment produce a hit-count larger than 15,000 rays in the norther half of the model, but decreasing to less than 5,000 at its southern end most importantly in the deepest G3, M1 and M2 layers. The Spread-Point Function (SPF) is build from the off-diagonal terms of the inversion kernel and therefor indicative of the resulting travel-time variations for a given velocity variation when taking the different ray paths into account. Similarly, the depth and velocity node SPF is asymetric in the model (Figure 7c), in the norther half generally lower than 3 and 5, respectively while in the southern half reaching 5 at the Moho and 8 for middle and lower crust, respectively. Finally, the diagonal terms of the resolution matrix is a measurement of the spatial averaging of the true earth structure by a linear combination of model parameters (Zelt, 1999). Typically, resolution matrix diagonals greater than 0.5–0.7 are said to indicate reasonably well-resolved model parameters (e.g., Lutter & Nowack, 1990). The major part of the interface and velocity nodes present good resolution (>0.7). Resolution is poorest between −180 and 15 km model distance at the base of middle and lower crust (Figure 7d). The total standard deviation for depth nodes and velocity nodes is 226 and 42.1 m/s, respectively.

4.3. Monte-Carlo Uncertainty Estimation

In order to assess the reliability and uniqueness of our final model, we explored randomly our model parameter space in the crustal and mantle layers using VMONTECARLO (Loureiro et al., 2016). The top of the crust G1 is fixed while the 54 depth nodes forming the base of the crustal layers G2 and G3 are randomly displaced vertically. The velocity nodes are allowed to vary from the top and base of the crust G1 to the upper-mantle M1, for a total of 25 upper velocity nodes and 24 lower velocity nodes. Fifty thousand random models were gener-

Table 2
Instrument Name, Distance Along Model, Direction Code (−1 for Rays Traveling Southward and 1 Traveling Northward), Number of Explained Events, Root Mean-Square Travel-Time Residual, and Normalized Chi-Square Value

Instrument	Position (km)	Direction	Npts	Trms (s)	Chi-square
MZ6OBS25	0.000	−1	1,732	0.089	0.439
	0.000	1	1,864	0.090	0.486
MZ6OBS24	12.460	−1	1,651	0.098	0.572
	12.460	1	2,109	0.168	1.536
MZ6OBS23	24.923	−1	1,221	0.081	0.337
	24.923	1	1,300	0.056	0.200
MZ6OBS22	37.348	−1	1,243	0.109	0.661
	37.348	1	1,366	0.060	0.176
MZ6OBS21	49.811	−1	1,205	0.058	0.184
	49.811	1	794	0.047	0.158
MZ6OBS20	62.231	−1	1,232	0.070	0.299
	62.231	1	1,186	0.099	0.518
MZ6OBS19	74.727	−1	1,689	0.104	0.495
	74.727	1	1,356	0.061	0.208
MZ6OBS18	87.116	−1	1,188	0.078	0.335
	87.116	1	1,606	0.104	0.627
MZ6OBS17	99.542	−1	1,212	0.066	0.277
	99.542	1	2,254	0.068	0.256
MZ6OBS16	111.959	−1	1,560	0.109	0.538
	111.959	1	1,323	0.033	0.065
MZ6OBS15	124.426	−1	1,144	0.093	0.478
	124.426	1	1,599	0.067	0.256
MZ6OBS14	136.911	−1	1,299	0.079	0.406
	136.911	1	1,459	0.067	0.281
MZ6OBS13	149.308	−1	1,120	0.079	0.355
	149.308	1	1,604	0.100	0.561
MZ6OBS12	161.872	−1	1,061	0.067	0.257
	161.872	1	1,256	0.051	0.145
MZ6OBS11	174.186	−1	1,056	0.091	0.452
	174.186	1	1,640	0.060	0.222
MZ6OBS10	186.502	−1	925	0.085	0.347
	186.502	1	470	0.081	0.258
MZ6OBS09	198.905	−1	932	0.065	0.254
	198.905	1	868	0.064	0.223
MZ6OBS08	210.351	−1	678	0.058	0.207
	210.351	1	818	0.061	0.227
MZ6OBS07	224.184	−1	715	0.054	0.132
	224.184	1	741	0.039	0.076
MZ6OBS06	236.751	−1	1,299	0.039	0.083
	236.751	1	765	0.043	0.090

ated with maximum velocity variation at each node of ±0.5 km/s and maximum depth variation of 2, 3, and 4 km at the base of G1, G2, and G3 (Moho), respectively and using the Metropolis algorithm and adaptive variance to increase the convergence. Furthermore in order to finely explore the model space near our final model, a pyramidal scheme was implemented, increasing in 10 steps the allowed depth and velocity variation from 20% to 100% of their maximum during the first half of the random model generation. During the second half, the maximum variations were only limited by the adaptive variance that targets an acceptance ratio of 23%. The first quality threshold used to establish the model ensemble was set to 75% of the final model's quality of fit, together with thresholds of 80% explained picks, 175% of the chi-square and 110% of the RMS (104.5 ms) of our final model. A global uncertainty map was then generated from the 95 random models that meet these thresholds (Figure 8A).

The velocity uncertainty is generally lower than ±0.25 km/s except in the vicinity of the Moho where the final model presents the strongest velocity contrast of ±0.94 km/s: the ±4 km depth variations and strong velocity contrast between lower crust and upper mantle transcribe into large velocity variations in order to meet our quality threshold.

Finally at six location along MZ6 profile, vertical slices through the explored model space are taken, where velocity profiles of the 50,000 random models are plotted color-coded according to their normalized average score together with four constant depth (10, 20, 30, 40 km) and four constant velocity (6.5, 6.9, 7.3, 7.9 km/s) profiles and their respective 95% confidence bounds (Figure 8B). At all local analysis locations, random velocity variations larger than 0.25 km/s all lead to normalized scores lower than 0.25. The width of the 95% confidence velocity bound rarely exceeds ±50 m/s. The depth bound is very narrow (generally less than ±500 m but reaches 1 km at 257 km model distance) for the 6.5 km/s constant velocity profiles as the velocity gradient in the upper crust G1 is higher than in the middle and lower crust. For the 6.9 profile, the depth bound is in the ±1 to ±1.75 km range. In our preferred model, a velocity of 7.3 km/s is reached only in the G3 layer north of 80 km model distance, and the depth bound in this area is in the ±1.5 to ±2 km range. Finally for 7.9 km/s constant velocity profiles, the depth bound is laterally homogeneous and in the ±1.5 to ±1.75 km range.

5. Seismic Stratigraphy

The stratigraphy at the NNV, MCP, and Limpopo margin has been established by Baby (Baby, 2017; Baby et al., 2018) and at a larger scale by Ponte (Ponte, 2018; Ponte et al., 2019), in collaboration with TOTAL, from a large seismic reflection and borehole data set. We have reappraised this stratigraphy along the E-W portion ~300 km in length of the "Section A" industrial seismic profile of Baby (2017) and Baby et al. (2018) in light of the MOZ3-5 WAS analysis (Figure 9; see Figure 1 for location).

At the base of the sequence, lying on top the crustal basement roughly identified on the WAS records, is the so-called Karoo volcano-sedimentary basin (the brown sequence on Figure 9); large areas of the south African and Antarctica continents were flooded by intense magmatism between 183 and 178 Ma-ago (e.g., Cox, 1992; Jourdan et al., 2005). U–Pb zircon (and baddeleyite) ages for 14 samples taken from sills across the Karoo Basin range from 183.0 ± 0.5 to 182.3 ± 0.6 Ma (Svensen et al., 2012). However, more varied ages were reported for the volcanics (from K/Ar-285.6 ± 14.3 to 116.8 ± 8 Ma; Flores, 1964), indicating

Table 2
Continued

Instrument	Position (km)	Direction	Npts	Trms (s)	Chi-square
MZ6OBS05	249.195	−1	982	0.041	0.102
	249.195	1	715	0.063	0.250
MZ6OBS04	261.681	−1	1,557	0.051	0.126
	261.681	1	479	0.066	0.303
MZ6OBS03	274.117	−1	1,362	0.077	0.722
	274.117	1	313	0.031	0.113
MZ6OBS02	286.566	−1	1,825	0.087	0.503
	286.566	1	307	0.039	0.101
MZ6OBS01	298.973	−1	1,535	0.050	0.194
	298.973	1	169	0.025	0.075
MZ6OLSS21	342.647	−1	1,755	0.108	0.851
MZ6OLSS20	342.647	−1	1,813	0.118	0.988
MZ6OLSS19	347.538	−1	2,720	0.057	0.207
MZ6OLSS18	352.454	−1	2,619	0.052	0.143
MZ6OLSS17	357.175	−1	2,608	0.107	0.764
MZ6OLSS16	362.466	−1	1,608	0.079	0.313
MZ6OLSS15	367.542	−1	2,212	0.077	0.235
MZ6OLSS14	372.525	−1	1,889	0.133	0.864
MZ6OLSS13	377.841	−1	2,832	0.117	0.519
MZ6OLSS12	382.732	−1	2,046	0.114	0.787
MZ6OLSS11	387.190	−1	2,348	0.106	1.046
MZ6OLSS10	392.705	−1	2,449	0.120	0.624
MZ6OLSS09	397.515	−1	1,891	0.096	0.587
MZ6OLSS08	402.204	−1	2,439	0.128	0.904
MZ6OLSS07	407.331	−1	3,039	0.101	0.510
MZ6OLSS06	414.119	−1	1,714	0.100	0.688
MZ6OLSS05	417.628	−1	2,656	0.073	0.275
MZ6OLSS04	424.533	−1	2,642	0.113	0.511
MZ6OLSS03	427.165	−1	1,758	0.098	0.471
MZ6OLSS02	431.049	−1	3,013	0.128	0.633

magma may not have been emplaced in one single event. Several wells (Sunray-1, 2, 3, 4, 7, 12, Funhalouro-1, Palmeira-1, Macia-1x, Nhamura-1; see Figure 1 for location) penetrated this volcanic unit at their base (Flores, 1964, 1973; Salman & Abdula, 1995). In these wells, recent dating of cuttings reveal Karoo (183 Ma) basalts at the base of the Nhachenge well, and both Karoo and Bombeni-Movene (140 Ma) basalts at the Funhalouro-1, and Sunray-12 wells; Also, Sr/Nd analysis shows that theses basalts sampled in the wells have neither a composition of MORB nor SDRs (Revillon, 2019). We interpret the (brown area) deep reflectors in NNV and the Limpopo Basin as pre-drift continental sedimentary or volcano-sedimentary layers, deposited into intracratonic sag basins, with superimposed possibly Triassic faulting (Guillocheau & Liget, 2009).

Above lie the continental Red Beds and the shallow marine Maputo formation. The Red Beds were dated at Neocomian age, and the Maputo Fm. were dated Barremian to Early Aptian (Baby et al., 2018) and Vlanginian to early Aptian (Said et al., 2015; Salman & Abdula, 1995). While the Red Beds are restricted regionally, the Maputo Fm. (yellow sedimentary layer) was identified north-eastward of Profile A over the zone of crustal uplift that flanks the Limpopo margin and on an anomalous crust (~6 km thick crust with a continental affinity) positioned west Mozambique Fracture Zone limiting the oceanic Mozambique Basin (e.g., Evain et al., 2021), giving an age older than the one of the oceanic crust at these latitudes, that is, of about 150–145 Ma. This formation presents progradational sequences infilling onshore rifts and faulted structures, offshore flexuration and early drifting basins. They are characterized by subparallel reflectors, onlapping the hangingwall dip slope offshore, and progradational infilling of remnant rift depression onshore. The main depocenters of this horizon are located in the inner margin rift depressions onshore on the MCP. In the NNV, the Maputo Formation represents the initial flooding of the shelf in the Early Cretaceous. The Neocomian unconformity (the unconformity between the Maputo Fm. and the Red Beds) is interpreted to mark a period of uplift and formation of oceanic offshore Mozambique Basin. The top of this sequence could represent the Late Aptian Unconformity (Salman & Abdula, 1995), and corresponds to the stop of Madagascar's drift from East Africa.

Above, the Lower Domo Shales (Figure 9, blue unit) represents progressive progradational infilling of the relief of the margin created during the Turonian uplift (Baby, 2017). It forms a post-rift sedimentary wedge onlapping toward the continent, representing a major mid-Cretaceous transgression of the shelf imaged on the seismic profiles (Figure 9) as continuous high-amplitude, parallel reflectors that locally exhibit low-angle clinoforms downlapping onto the Maputo Fm., dominated by marine mudstones with some bands of arkosic sandstones (Salman & Abdula, 1995). The thickness of this formation increases considerably on Profile A (Figure 9) within the Chedinguele Graben, active during the Early Cretaceous (Raillard, 1990; Sahabi, 1993; Watkeys, 2002) and possibly until the Campanian-Maastrichtian deposition of the Lower Grudga Fm.

Unconformably overlying the Lower Domo Shales is the Domo Sandstone, a sandprone interval most developed in the central portion of Profile A. It is a reflective sequence of high amplitude and continuous reflectors containing late Cenomanian-Mid Turonian fauna (Salman & Abdula, 1995). In this unit, acoustic velocity reach locally 4–4.5 km/s along the MZ7 and MZ3 profiles at or near the vicinity of their intersection with Profile A (1-D velocity-depth profiles inlet in Figure 9).

Above, the Upper Domo Shale are composed of overall regressive dark gray, marine shales and clays interbedded with thin glauconitic sandstone and siltstone beds (Salman & Abdula, 1995). The formation is typically 600–650 m thick coarsening upwards with aggradational continuous, high amplitude reflectors. The top of this sequence marks a regionally intra-Senonian Unconformity. Sunray-2 and 4 terminated in basic intrusives within the Upper Domo Shale. The intra-Senonian unconformity (between the Domo Sand and Upper Domo Shale)

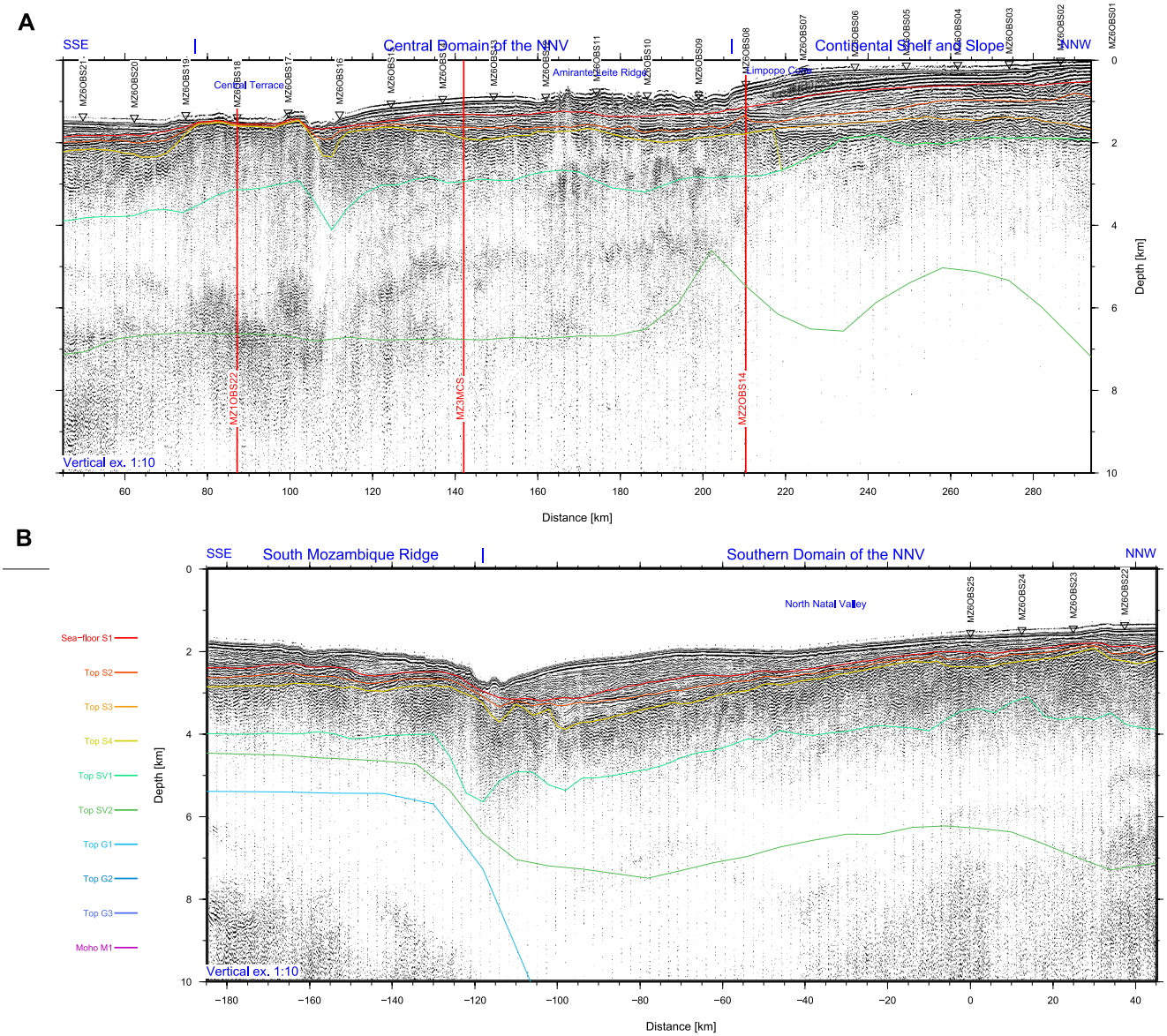

Figure 6. Pre-stack depth migration of the MZ6MCS data. (a) Northern portion; (b) Southern portion; Model's interfaces are represented with continuous lines. The intersections with the MOZ3-5 data set are indicated by red line. OBS location are indicated by white triangle. Vertical exaggeration is 1:10.

corresponds to C34 a period that saw the breakup between India and Madagascar, and Australia and Antarctica (e.g., Thompson et al., 2019).

This sequence is topped by the thick lower Grudja claystone and Grudja shaly marl. The Early Eocene unconformity corresponds to a stop of accretion in the Mascarene basin at C27, and a ridge jump to initiate seafloor spreading between Seychelles and India at C27 with the arrival of the Reunion hotspot initiating the Deccan Traps of India (66 Ma) and the basalts on the Seychelles micro-continent (62.4 ± 0.9 Ma, Shellnutt et al., 2017).

Then follow the Cheringoma formation, deposited during the Middle to Late Eocene, and characterized by stacked nummulitic limestones with bands of clay and calcareous sandstone and the Late Miocene Jofane formation, characterized by marine carbonates: limestone, calcarenite, and arenaceous limestone (Salman & Abdula, 1995). It topped by Neogene shales, nearly transparent on the seismic section.

Varied ages were reported for the volcanic episodes (from K/Ar-285.6 ± 14.3 to 116.8 ± 8; Flores, 1964). U–Pb zircon (and baddeleyite) ages for 14 samples taken from sills across the Karoo Basin range from 183.0 ± 0.5 to 182.3 ± 0.6 Myr

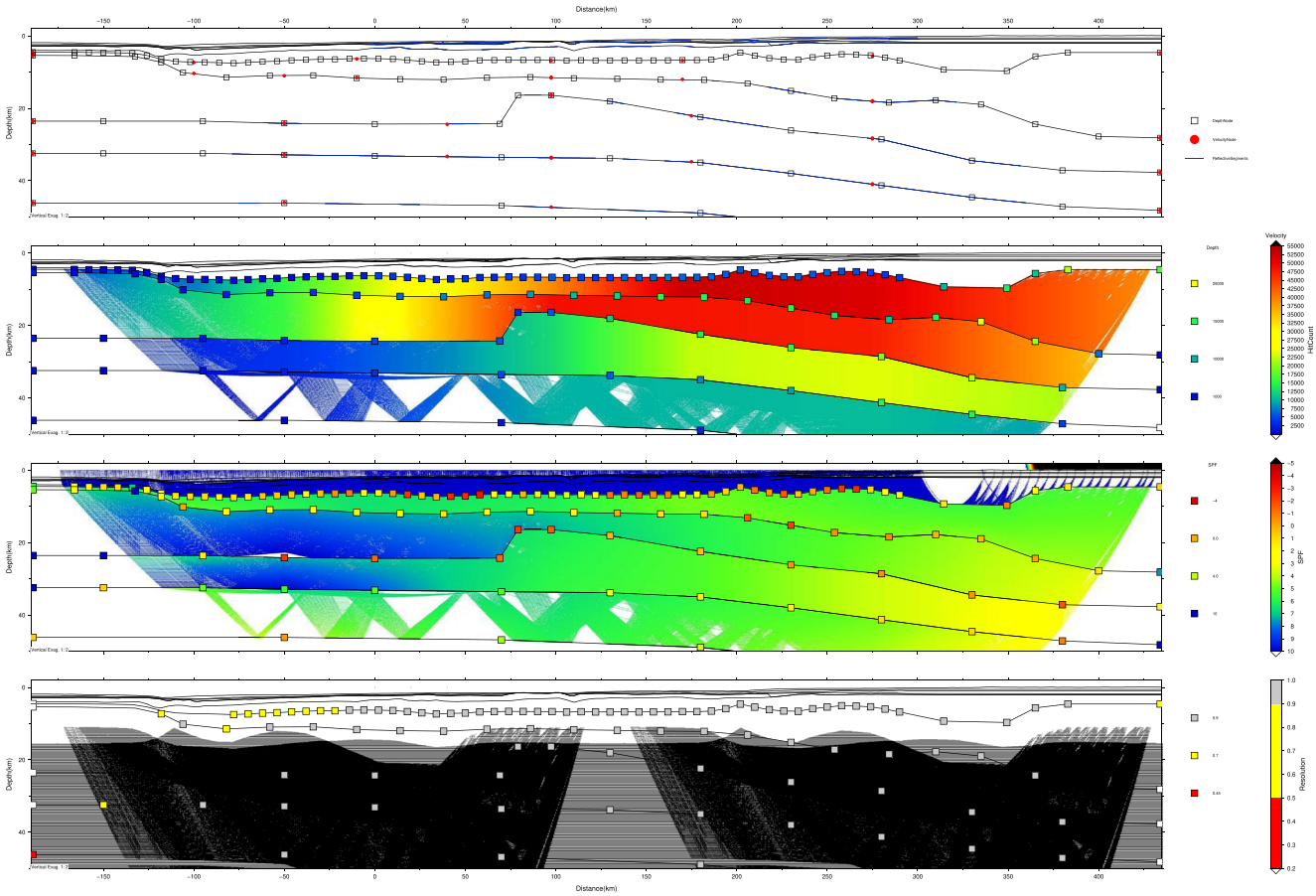

Figure 7. Evaluation of the wide-angle model MZ6. (a) Model parameterization includes interface depth nodes (squares), top and bottom layer velocity nodes (red circles); interfaces where reflections have been observed on OBS data are highlighted in blue. (b) Hit-count for velocity (colored) and depth nodes (squares). (c) Smearing from Spread-Point Function for velocity (colored) and depth nodes (squares). (d) Resolution of velocity (colored) and depth nodes (squares). Zones that were not imaged are blanked.

(Svensen et al., 2012). Recent dating of cuttings reveal Karoo (183 Ma) basalts, at the base of the Nhachenge well, and both Karoo and Bombeni-Movene (140 Ma) basalts at the Funhalouro-1, and Sunray-12 wells, and the Sr/Nd analysis shows clearly that the basalts sampled in the drill have neither a composition of MORB nor SDRs (Revillon, 2019).

6. Discussion

6.1. Vertical Velocity Cross-Sections

Furthermore, in order to characterize the P-wave seismic velocity variations along the MZ6 profile, 1-D velocity-depth profiles were extracted from the velocity model at 10 km interval (Figure 11): 1-D velocity-depth profiles below the seafloor allow to discuss the lateral variations in the geometry of the sedimentary layers and their relation to the stratigraphy, while 1-D velocity-depth profiles below the basement allow to discuss the properties of crust.

The model's 4 upper layers reach a thickness of 2.5 km in the Limpopo Cone (S1 to S4; Figures 5, 6, and 10). The S1 top/bottom velocity ranges from 1.6/1.7 km/s on the shelf, 1.75/1.85 km/s at the ALR, to 1.75/1.8 km/s onshore. The S2 top/bottom velocity is 1.8/1.9 km/s offshore and increases to 2.4/2.45 km/s onshore. Similarly, The S3 top/bottom velocity is 1.95/2 km/s south of 210 km model distance (continental slope) and increases to 2.5/2.55 km/s onshore. The average S4 top/bottom velocity is 2.45/2.50 km/s increases to 2.6/2.65 km/s onshore. The seismic reflection signature and the range in acoustic velocity (generally less than 2.65 km/s) clearly indicates the sedimentary nature of S1–S4 layers. This remarkably low velocity is puzzling given the time-span of deposition, and suggests under-compacted strata. As a matter of fact, the pediplanes of the southern African continent underwent continuous denudation during the Cretaceous and Cenozoic times, producing large amount

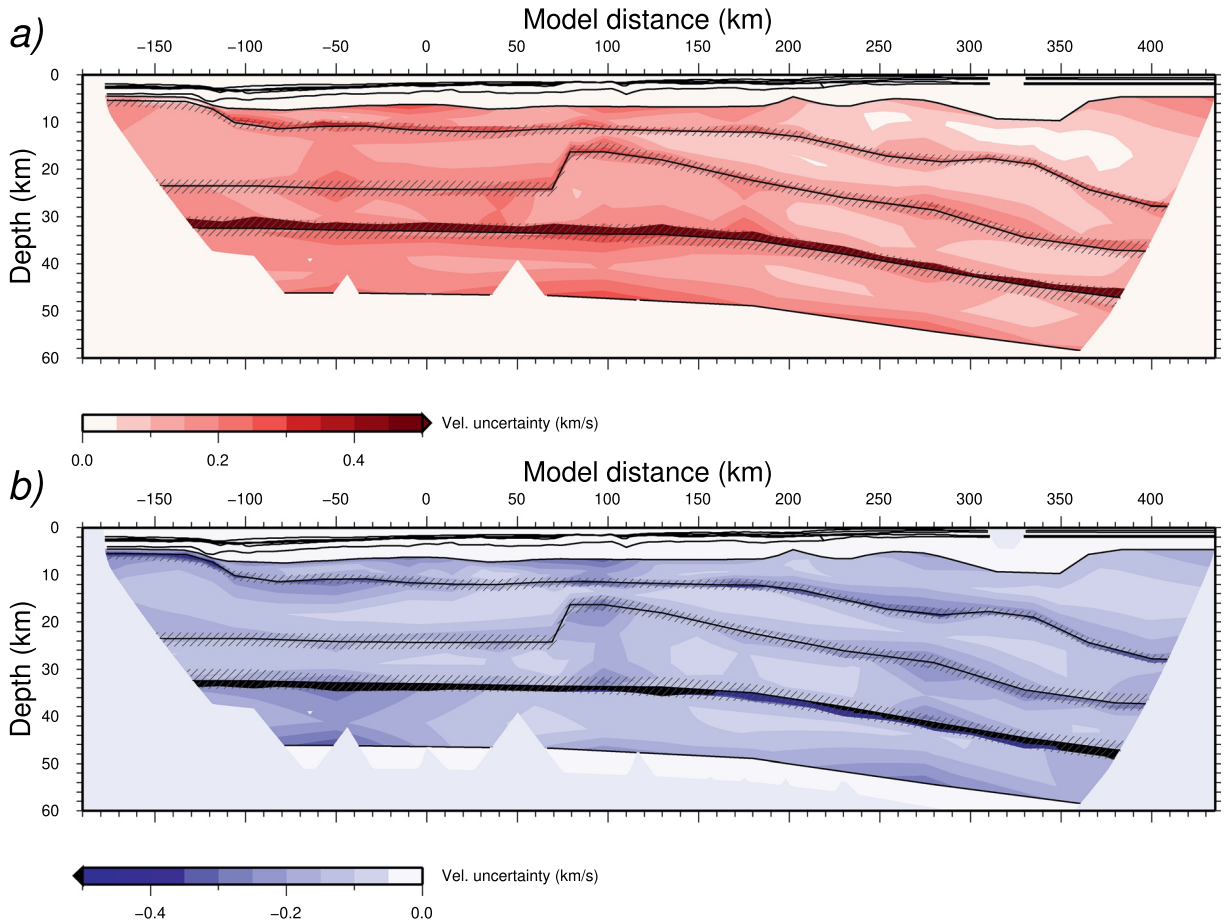

Figure 8. (A) Global uncertainty map generated from the standard deviation of the 94 random models meeting our thresholds. Crust and mantel portion of our final wide-angle model MZ6. (a) Positive velocity uncertainty. (b) Negative velocity uncertainty. The hashed area indicate the standard deviation of the depth of interfaces explored during the Vmontecarlo. (B) Vertical slices through the model space at −115, −22, 71, 164, 257, 350 km model distance. (a) Four constant depth (10, 20, 30, 40 km) profiles are extracted from the normalized scores of the random models and the 95% confidence velocity bounds are plotted with dashed lines. (b) Normalized scores of the 50,000 random models. (a) Four constant velocity (6.5, 6.9, 7.3, 7.9 km/s) profiles are extracted from the normalized scores of the random models and the 95% confidence velocity bounds are plotted with dashed lines.

of laterite, and resulting in a dominant kaolinites and smectite rich shales export offshore (Guillocheau, 2019). The shale-rich deposition together with later diagenesis in the marine environment may explain the unusual low velocity range of these S1 to S4 deposits. The sedimentary cover further thins down southward.

From the MCP to CSS, the SV1 and SV2 strata above the basement thins from 9 km down to 4 km—primarily the SV2 layer that presents a lower velocity gradient onshore. Southward, the total thickness of SV1&2 is preserved throughout the C-NNV at about 6 km. In the S-NNV, SV1&2 further thins to 4 km thickness, presenting slightly higher velocities at the base of SV2. At the ALR, characterized by 0.5–5 km wide corrugated mounts outcropping from the sedimentary cover on the bathymetry (Figure 3), the gathers remain relatively well focused from sea-bottom to the SV2 horizon and the seismic section suggests relatively narrow vertical dykes piercing the sedimentary and SV1 strata (Figure 2); the wide-angle velocity above SV1 is not higher at the ALR than northward at the CSS. The SV1 top/bottom velocity is 3.8/4.9 km/s though out the model, except at the center of the ALR (3.4 km/s at the top) and the northern edge of SV1 (3.55/4.3 km/s). The range of velocity together with the wavy and scattered seismic reflection pattern suggests volcano-clastic SV1 strata with possible increasing magma content with depth. The SV2 top/bottom velocity ranges from 5/6.3 km/s south of 50 km model distance (NNV and MozR), decreasing to 4.5/5.9 km/s at the shore-line. The range of velocity, the transparent seismic reflection signature and large scatter on the CIGs together with poor focusing of their semblance suggest higher magmatic content.

At the MCP and CSS, the tie of S1–S4 is relatively straightforward (Figure 10): S1 would include the Neogene, Cheringoma and Jofane Fm., and Upper Grudga units, S2 the Lower Grudga and Upper Domo Shales, S3 the

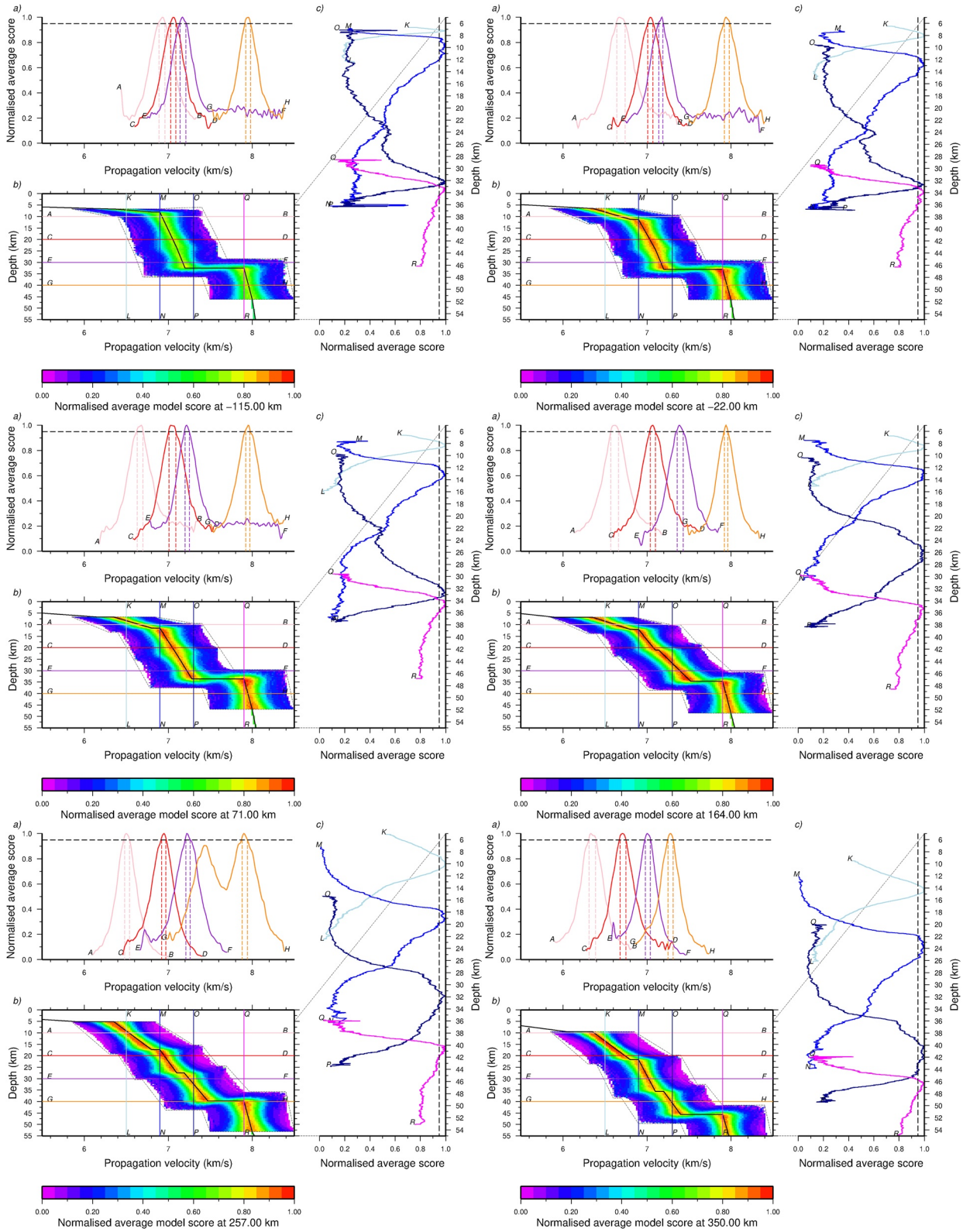

Figure 8. (Continued)

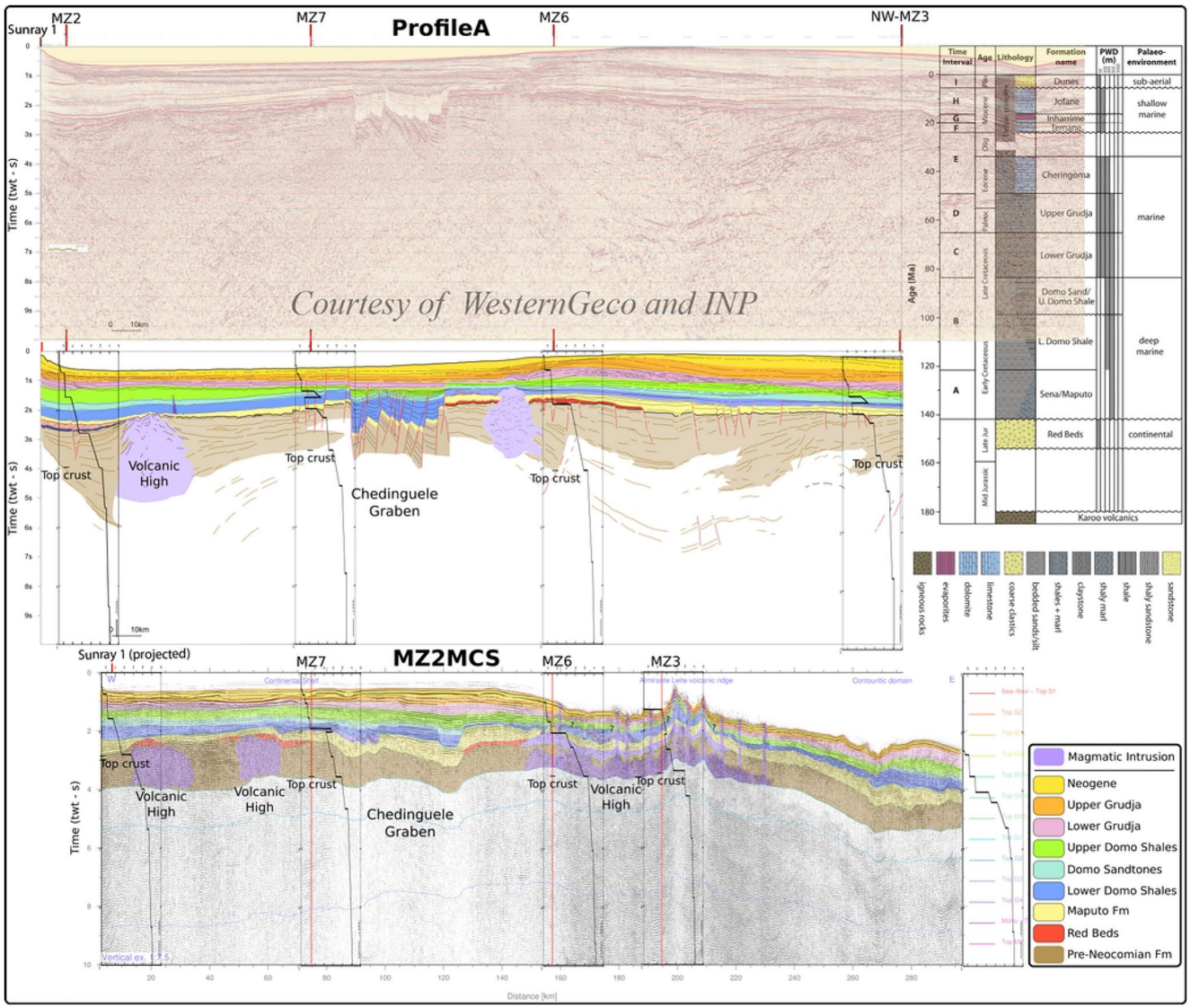

Figure 9. (a) Two-way travel-time line drawing of the Profile A and interpreted faults. (b) Profile A stratigraphic interpretation. (c) Record section of MZ2MCS, overlain by time converted interfaces of wide-angle model and our stratigraphic interpretation. The intersections with the MOZ3-5 data set are indicated by red line, and the 1D velocity profile of the intersecting profile is presented as inlet. MZ2 western and eastern-most 1D velocity profile are presented as inlets. Vertical exaggeration at seafloor is 1:7.5. Composite stratigraphic column of the Mozambique marginal Basin (after Said et al. (2015) modified after Salman and Abdula (1995)), with indication of the paleo-water depth and the paleo-environment.

Domo Sandstones and Lower Domo Shales, S4 the Maputo Fm. and Red Beds. SV2 comprises the so-called Karoo volcano-sedimentary unit. As the age is unknown, we herein prefer to name the SV2 unit the "Pre-Neocomian Fm." (topped by the Neocomian Red Beds). Southward, the stratigraphy of S1 to S3 can be extended to the CT with reasonable confidence, given the seismic signature, major unconformities, and acoustic velocities. At the CT, the SV1 unit outcrops over a wide area of the NNV (Figure 3): extending our stratigraphic tie from the Sunray-1 well to the S-NNV and the MozR is, in our opinion, not sufficiently reliable with our set of data. However, recent biostratigraphic results indicate that the lower sedimentary section of DSDP Site 249, located 100 km SE of MZ6 profile (Figure 1), is no older than Barremian (Dunay et al., 2018), suggesting that the Post-Neocomian sequence observed at the MCP may have deposited at the GP reaching 406 m thickness.

Southward of 220 km model distance, the S4 sequence is replaced by the SV1 unit. Below, the SV2 unit is continuous in thickness, seismic character (discontinuous reflector, poor semblance), velocity and velocity gradient across not only the S4/SV1 contact but southward to the CT and S-NNV. The contact between S4 and SV1 indicates that the deposition of the S4 strata is either contemporary or post-dates the magmatic SV1 event. Therefore, the S4/SV1

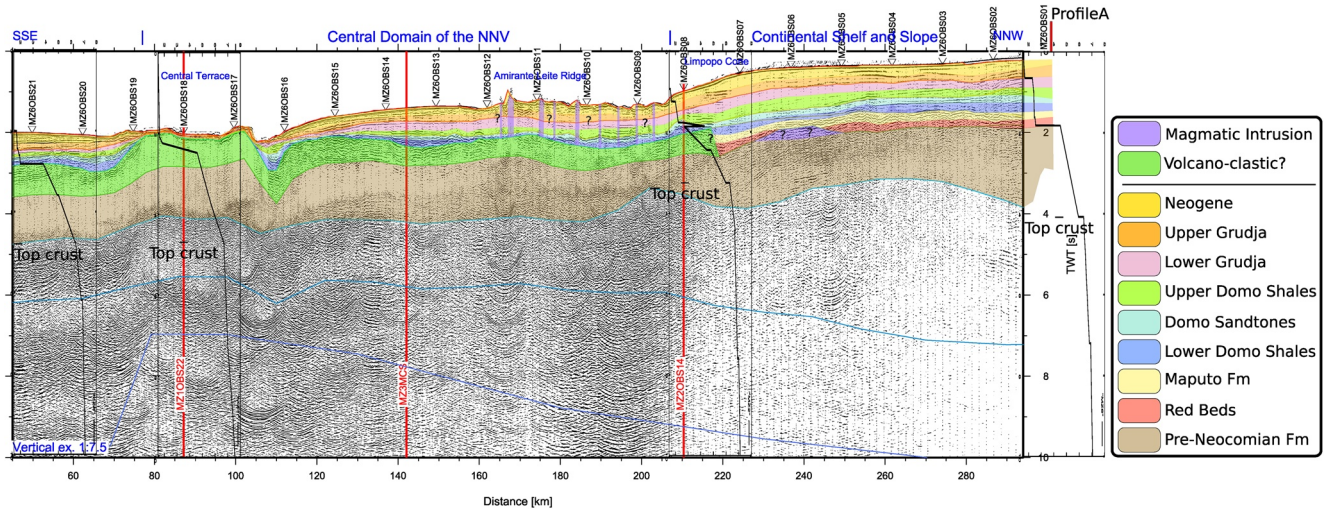

Figure 10. Two-way travel-time record section of MCS data along MZ6 profile overlain by time converted interfaces of wide-angle model and our stratigraphic interpretation. The intersections with the MOZ3-5 data set are indicated by red line, and the 1D velocity profile of the intersecting profile (when available) is presented as inlet. MZ6 norther and southern-most 1D velocity profile are presented as inlet. OBS location are indicated by white triangle. Vertical exaggeration at seafloor is 1:7.5.

contact raises two scenario: (a) the SV1&2 form a single unit, where more intense Movene magmatism emplaced a broad plateau, almost 1,000 m high where the Red Beds and Maputo Fm. was restricted to the MCP until the gap to this plateau was closed. (b) The S4 and SV1 units are synchronous, but the magmatism lasted longer at the CSS & NNV than at the MCP, resulting in a lateral seismic signature/velocity change. Two observations, however, favor the second scenario: the S4/SV1 detailed contact, and the stratigraphy of the S3 overlying strata. The transition between the S4 and SV1 is gradual in both seismic signature and velocity (from 2.65/3.0 at 215 to 4.25/4.85 km/s at 200 km model distance). Then, the WAS velocity reaches locally 4.6 km/s in the sand prone Domo Sands on the MZ2 profile at the crossing with MZ6, 200 m above the top of SV1 (Figure 10), and northward on MZ3 at the crossing with MZ2. Therefore, the magmatic event may have lasted at most into the period of deposition of the Lower Domo Shales (121-99 Ma), which drape and locally fills topographic lows of SV1, on either sides of the CT for example, Furthermore, between 30° and 35°S, large volumes of magma where emplaced at the aseismic south MozR (e.g., Fischer et al., 2017; Gohl & Uenzelmann-Neben, 2001; Gohl et al., 2011). Based on geophysical (seismic and magnetic) data and a kinematic reconstruction, the MozR formed at a triple junction during multiple events, in the north at 135 Ma and continued to grow toward the southwest, where the central area formed mainly at ca. 131 Ma and volcanism lasting until ca. 126 Ma at the southwestern sub-plateau and ca. 125 Ma at less prominent SE plateau (Fischer et al., 2017; König & Jokat, 2010). The geochemical analysis of 55 dredges collected on the upper (exposed) part of the plateau led to two possible models for the magmatism at the south MozR (Jacques et al., 2019): (a) formation by a "second" mantle upwelling (blob or mantle plume) that followed the Karoo and Bumbeni-Movene groups, possibly reflecting a pulsating plume, or (b) melting of subcontinental lithospheric material transferred by channelized flow to the mid-ocean ridge shortly after continental break-up in ridge-ridge-ridge type Triple Junction (Georgen, 2008). Both models could apply northward in the NNV.

Finally, south of the CT at the S-NNV, the SV1 strata presents clear southward (seaward) dipping; from the seismic section, it is unclear whether the geometry of SV1 was acquired in a host and graben system as no clear normal faults are imaged or though regular spacing of extrusion centers of magamatic dykes. The southward bending of the S-NNV might have originated from tectonic thinning of its basement prior or during the SV1 event. At −55, 0, and 210 km model distance, both S3 and part of S2 appear disturbed up to the top of the Upper Domo Shales (c.a. 99 Ma), suggesting a late (Turonian) magmatic pulse. However, the dykes piercing though S3 and S2 at −55, 0, and 210 km model distance may have originated during a later event, without sufficient magama to reach the sub-surface. At the ALR between 160 and 200 km model distance, the highly reflective and flat layered S2 and S3 sequence are only very locally truncated by vertical seismic blanking. Above, the more transparent S1 layer is considerably disturbed and partially replaced by magmatic products. Thus at the ALR, the latest magmatism may have occurred during the deposition of S1 or present times. As a matter of facts, glasses dredged at the ALR during the MOZ3-5 survey were dated at 1.5 Ma (Berthod & Bachèlery, 2019). Finally, evidence for widespread post-sedimentary magmatic activity at the NNV (Hartnady et al., 1992) and the south MozR (Fischer

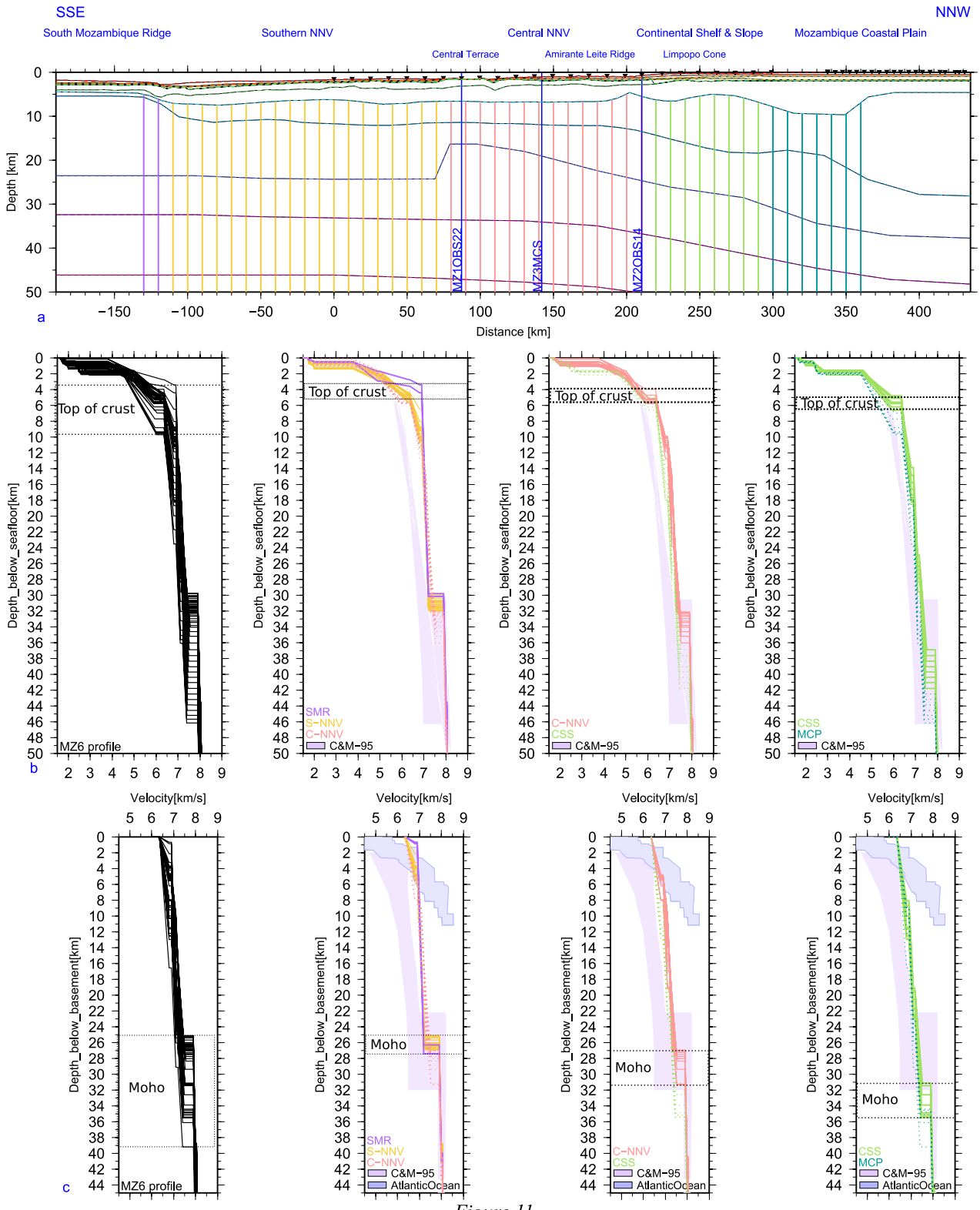

Figure 11

Figure 11. (a) Distribution of 1-D velocity profiles extracted from the final P-wave interval velocity model and color coded according to segmentation along the MZ6 profile. (b) P-wave interval velocity as a function of depth below seafloor. (c) P-wave interval velocity as a function of depth below basement and compared with compilations from the literature for continental crust from Christensen & Mooney, 1995 (C&M-95 in magenta), and Atlantic oceanic crust from White et al., 1992 (W-92 in blue).

et al., 2017) have been correlate with a southward propagation of the East African Rift System, of which the ALR could be part of (O'Connor et al., 2019).

6.2. Crustal Nature

The crustal nature of the MCP, NNV, and MozR has been much debated for its impact on reconstruction models of Gondwana (see Thompson et al., 2019 for a review). Two contrasting models have been proposed. The first model implies a partly continental (e.g., Ben-Avraham et al., 1995; Eagles & König, 2008; Hartnady et al., 1992; Tikku et al., 2002) or an entire continental origin of this area including the MozR (e.g., Lafourcade, 1984; Mougenot et al., 1991; Raillard, 1990). Based on geomagnetic, gravity, and seismic studies, this model places the continent-ocean boundaries (COB) south of the Naude Ridge, for example, offshore Durban near the South Tugela Ridge (e.g., Darracott, 1974; Dingle & Scrutton, 1974; Martin et al., 1981; Scrutton, 1973), or near the AG as inferred by the sea surface vector geomagnetic analysis (Hanyu et al., 2017) and the WAS profiles of the MOZ3-5 survey (Leprêtre et al., 2021; Moulin et al., 2020), and it assumes that the NNV and Limpopo Corridor are continental or transitional crust. The seafloor spreading is dated at around 135 Ma from the magnetic anomaly of the deep-sea basin, when the Patagonia plate moved to the west, during the opening of the Austral segment of the South Atlantic ocean (Moulin et al., 2020). The second model favors an oceanic origin of the southern part of the MCP, the Natal Valley and the MozR, and places the COB within the MCP near the Lebombo and Mateke-Sabi monoclines (e.g., Cox, 1992; Eagles & König, 2008; Leinweber & Jokat, 2011; Nguyen et al., 2016; Reeves et al., 2016), although Leinweber and Jokat (2011) suggest that the eastern part of the MCP to be underlain by transitional crust. Recently, Mueller and Jokat (2019) shifted the COB southward within the NNV, mainly based on gravity and magnetic data. They consider two alternatives for the crustal nature at the southern MCP consisting either of thick oceanic crust (scenario 1), or of blocks of highly intruded stretched continental crust (scenario 2), which was captured from the Antarctic plate by a rift jump from the central MCP to the inner SDRs of the Explora wedge; in their scenario 2, which is partly based on their interpretation of our MZ6MCS profile, the COB is located between MZ6OBS07 and MZ6OBS08. In these scenarios (Mueller & Jokat, 2019), the NNV was formed between M26r to M18n (157.1–144 Ma) and the entire MozR between M18n, when, in the Mozambique Basin, the rift jumped from north to south of the Beira High, to M6n (144–131.7 Ma). The northern part of the SNV is formed by N-S directed spreading between Africa and Antarctica at M18n to M15n (144–139.6 Ma), whereas most of its southern part is related to the separation of South America. Finally, based on seismic reflection profiling of the south MozR, Fischer et al. (2017) propose later emplacement of the individual segments between 130.9 and 126.7 Ma (cMozR), 130.9–128.7 Ma (swMozR) and 125.9–124.9 Ma (seMozR). Nevertheless, in these models about the entire Northern and Southern Natal Valley as well as the MozR are floored by thick oceanic crust.

From the 1-D velocity-depth profiles extracted from our velocity model (Figure 11), the crust is characterized by minor variations in total thickness, the vertical velocity and velocity gradients of G1, G2, and G3 along the MZ6 profile. At most norther illuminated part of MZ6 profile (350 km model distance), the Moho lies at 46 km depth. Southward, between the MCP and CSS, the Moho rises to 37 km depth, the crust thinning from 39 to 31 km. In the C-NNV, the crust further thins down to 27 km and presents slightly higher velocities than at the CSS and MCP. Southward in the S-NNV, crustal thickness further thins from 27 to 25 km. The depth of G3 and the Moho southward of the NNV are fully constrained by our inversion to −120 and −110 km model distance, respectively (the norther edge of the MozR). At the MozR, a velocity higher than 6.9 km/s is needed less than 1 km below sea-floor in order to fit the P2g and PmP arrivals of the shots fired at the MozR and recorded by MZ6OBS24 and MZ6OBS25, and in order to fulfill a conservative hypothesis that the depth of the Moho is preserved; lower velocities would lead to greater Moho depth. The total crustal thickness increases from 26 to 28 km.

Along the MZ6 profile, the upper crust has a thickness that may reach 22 km onshore decreasing to ∼4 km at the southern portion of the NNV. The middle crust, characterized by continuous 6.9/7.1 km/s top/bottom velocity is ∼10 ± 3 km thick though out the model except from 70 (the CT) to 180 km model distance (the center of the ALR), thinning to 5 km under the CT. The lower crust, characterized by a velocity larger than 7.1 km/s, is ∼9 km thick at the S-NNV, up to 17 km at the CT, and thinning gradually to 10 km onshore. The bathymetric mounts and underling magmatic dykes (producing vertical seismic blank on MZ6MCS) observed at the ALR coincide with an area of unusually high velocity, reaching 7.45 km/s at the base of the lower crust. The CT is underlain by the highest overall crustal velocity (up to 7.5 km/s). The velocity reaches 7.6 km/s along MZ1 at the crossing with MZ6 (Figure 10; Moulin

et al., 2020). Finally, the crustal architecture along the MZ7 parallel profile (Leprêtre et al., 2021; Moulin et al., 2020) is very similar to MZ6 onshore (where the Moho lies at 45 km depth) and along the CSS and the Central Domain of the NNV, with a lower-crust velocity also reaching 7.5 km/s along MZ7, and evidence of volcanic events in the sedimentary sequences above, although without outcrops. However in the Southern Domain of the NNV, the crustal velocity along MZ6 drop more significantly than MZ7. Furthermore, the Moho rises from 33 km depth below the Naude Ridge to 15 km at the southern extremity of MZ7: this thinning is not observed at the MozR on MZ6 profile.

The comparison of the 1D velocity profiles with a worldwide compilation of the oceanic crust of the Atlantic Ocean (White et al., 1992) unsurprisingly shows clear dissimilarities: the 6.3 km/s velocity observed at the top of the crust is much larger and the total crustal thickness in excess of 25 km are not compatible with normal oceanic crust. At the south MozR, the AWI20050300 WAS profile (see Figure 1 for location) reveals an up to 22 km thickened oceanic crust (Gohl et al., 2011) where the lower two-thirds of the crustal column exhibit P-wave velocities of more than 7.0 km/s, increasing to 7.5–7.6 km/s at the crustal base. Interpreting some of the crust along MZ6 profile as thickened oceanic implies that the SV2 layer (and possibly SV1) as an oceanic crustal layer2 would reduce these dissimilarities at the cost of further thickening the crust. The MZ6 1D velocity profiles are more comparable with the compilations of the unthinned and thinned continental crust (Christensen & Mooney, 1995): our crustal thickness and velocity better fit worldwide continental margins; Velocities observed along the MZ6 profile are however 0.5–1 km/s higher than observed (generally) elsewhere, most particularly in the C-NNV (Figure 11c). Therefore, these high velocity, observed through-out this area on all four other WAS profiles of the MOZ3-5 survey, together with the magma-rich SV1&2 strata and volcanic extrusions observed at the MPC and NNV strongly suggest mantle-derived melts intrusions into a slightly thinned continental crust southward the MCP. Moreover, the observed lateral velocity variations together with the absence of large vertical velocity increase does not suggest the presence of tabular underplate at the base of the crust. Finally, the upper-mantle velocity throughout our model is mostly constrained Pn recorded by LSS onshore and by PmP2 recorded by OBS/LSS: we obtain a reasonably good fit with a constant 7.9/8.0 km/s top/bottom velocity of the upper mantle, but the Monte-Carlo evaluation of our model clearly shows that lateral velocity variations in the upper-mantle, possibly coincident with the magmatic intrusions, cannot be precluded.

7. Conclusions

The crustal architecture along MZ6 profile is segmented coincidentally with the bathymetric, sedimentary, magmatic intrusions, and seismic observations. It is very similar with that imaged along the <70 km distant MZ7 (Leprêtre et al., 2021) parallel profile, and can be summarized as:

1. The NNV underwent intense magmatism similar to that observed at the MCP during the Karoo and Bombeni-Movene events: a volcano-sedimentary pre-Neocomian Fm. (SV2) was emplaced on top of the crustal basement over both MPC and NNV. Based on our stratigraphic analysis, these phases of magmatism may have lasted up to c.a. 99 Ma to the latest, contemporary of the crustal thinning of the S-NNV and subsequent spreading between Africa and Patagonia.
2. The southern domain of the NNV presents volcano-sedimentary deposits and increasing magma content in depth very similar in thickness and characteristics (velocity and seismic signature) to the central domain of the NNV (ALR and CT), and a crustal velocity and velocity gradient similar to that imaged below the CSS but 5 km thinner (27 km at the NNV for 32 km at the CSS).
3. The bathymetric mounts and underling magmatic dykes observed at the ALR are the expression of the most recent magmatic stage in the NNV, possibly linked to a southward propagation of the East African Rift System. Furthermore, the ALR coincide with an area of unusually high velocity at the base of the lower crust.
4. The overall crustal thinning lies onshore MCP (200–350 km model distance) and below the CSS.
5. The CT presents the highest overall crustal velocity (exceeding 7.2 km/s below 17 km depth).
6. The crust along MZ6 profile, although very likely intruded by mafic melts, does not present evidences of upper-mantle tabular underplating.

Appendix A

Common image gathers of MZ6MCS, spaced every 14 km, and their residual move-out semblance plot are provided (Figures A1). Regarding our Monte-Carlo evaluation, a plot of interface depth nodes, upper velocity nodes, lower velocity nodes and locations of the vertical slices through the model space is shown (Figure A2).

The seismic record, seismic record overlain by predicted times, color coded synthetic, observed travel-times overlain by predicted times, seismic rays, and MCS time migrated section and color-coded model interfaces of all instruments deployed of the MZ6 profile are provided as supplementary data (Figures B1–B45 in Supporting Information S1). Table A1 summarizes the acronyms used in this study.

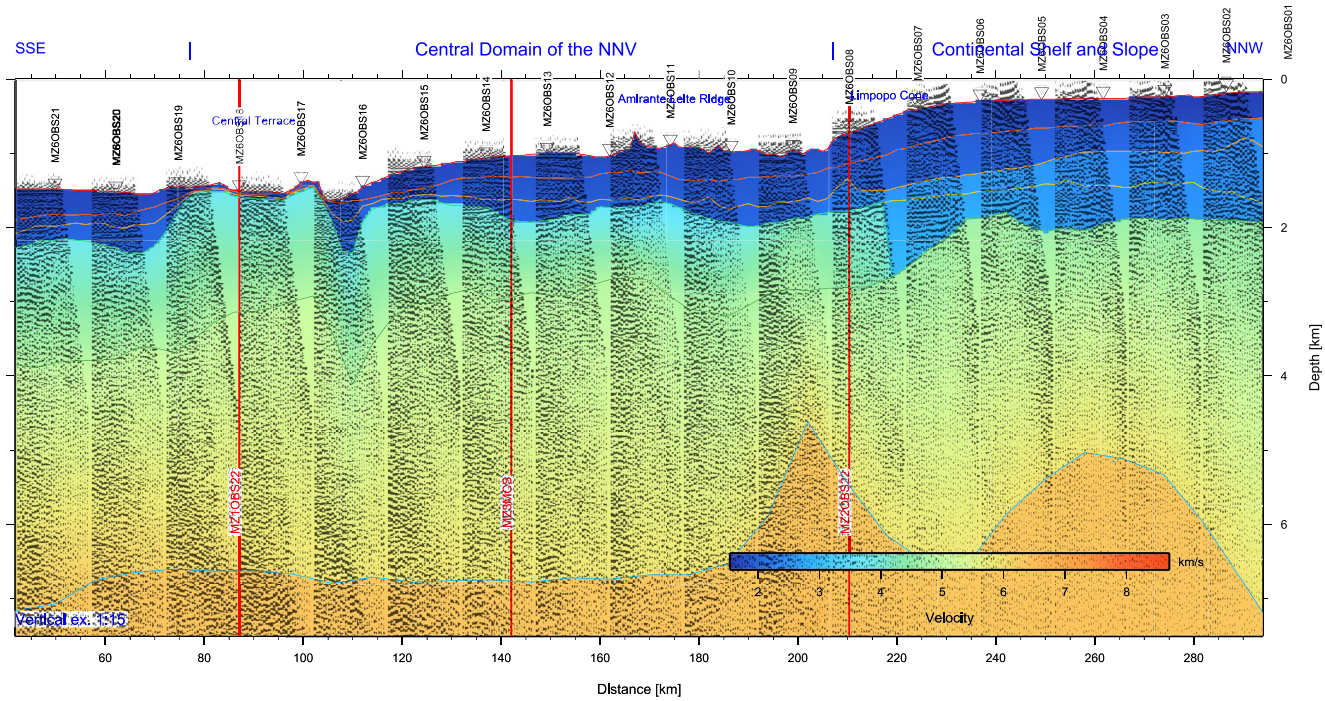

Figure A1. Pre-stack depth migration and residual move-out of the MCS data along MZ6 profile. (a) Northern portion; (b) Southern portion (a) Residual move-out. (b) Semblance plot of the RMO. Common image gathers are spaced every 14 km. Vertical exaggeration is 1:15. Model's interfaces are represented with continuous lines.

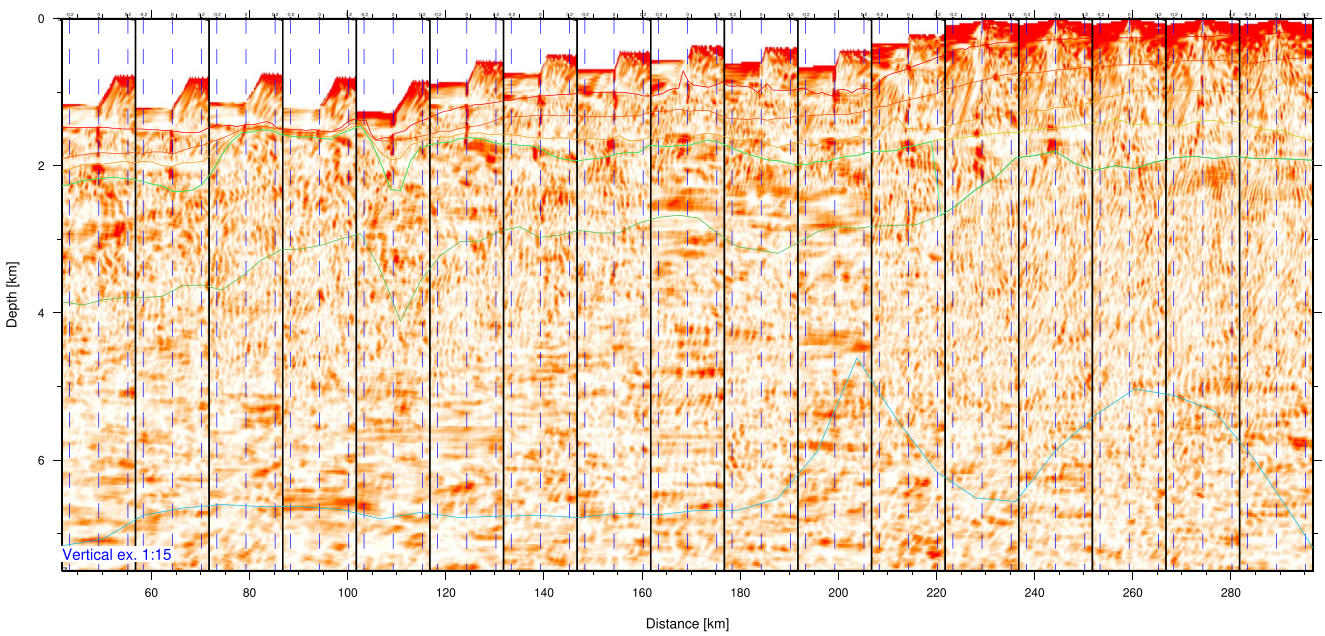

Figure A1. (Continued)

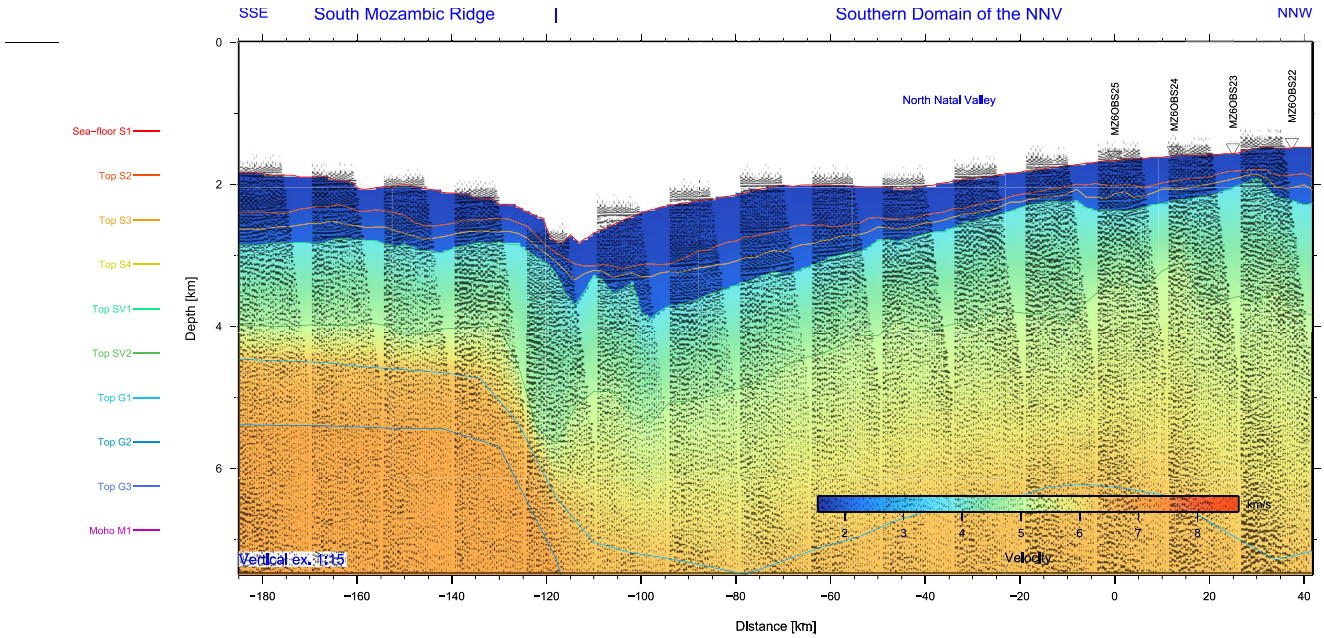

Figure A1. (Continued)

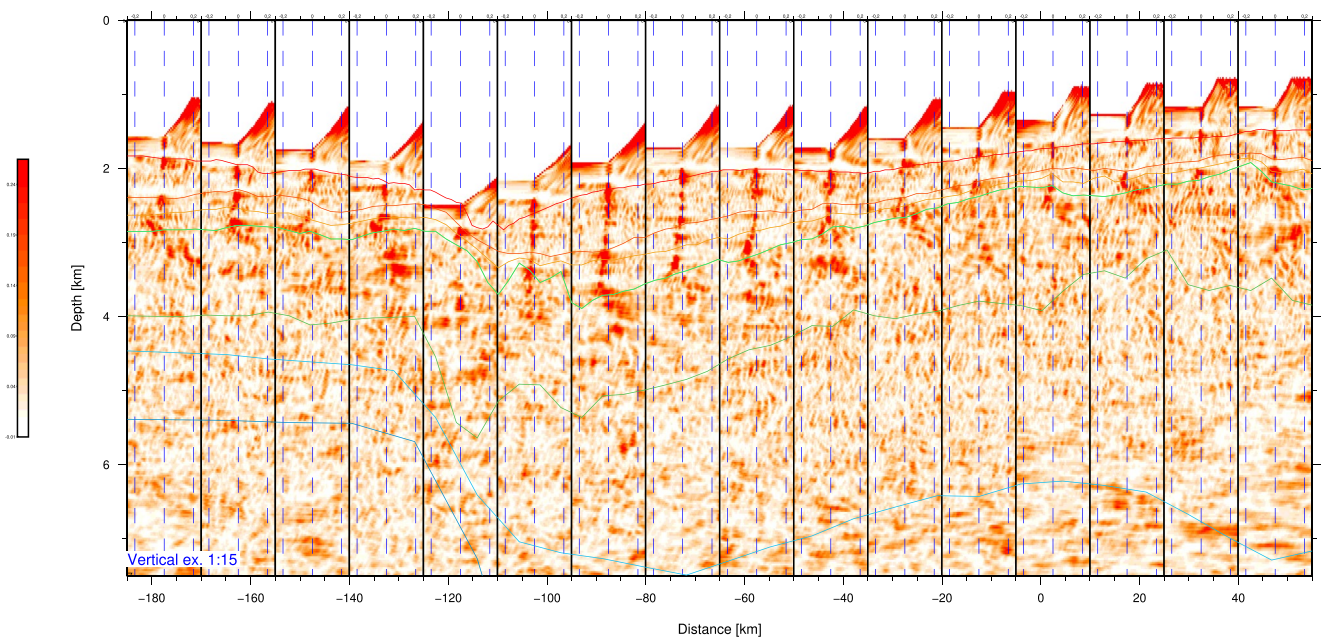

Figure A1. (Continued)

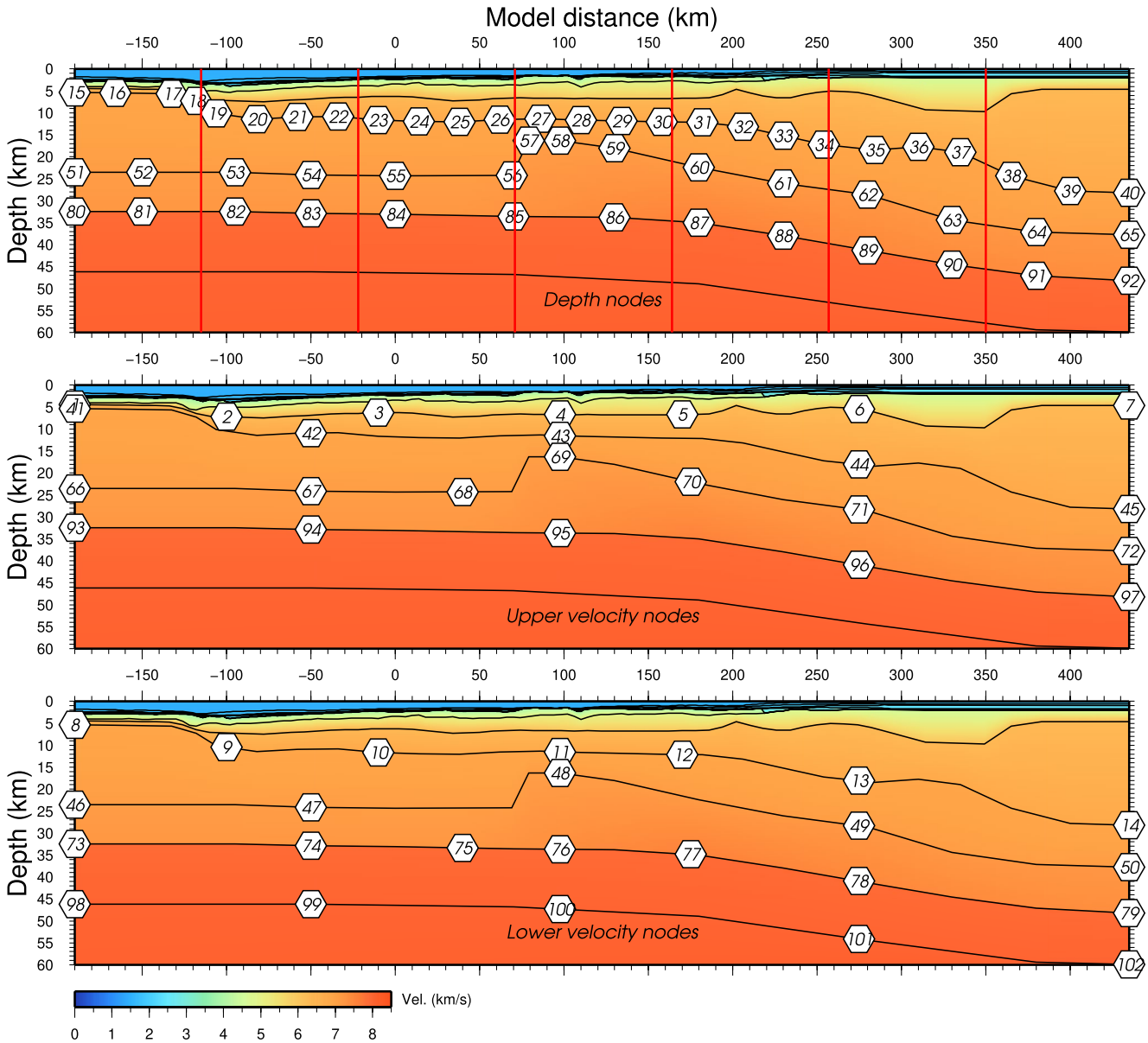

Figure A2. Vmontecarlo evaluation of the crustal and mantelic portion of our final wide-angle model MZ6. (a) Interface depth nodes. (b) Upper velocity nodes. (c) lower velocity nodes. The locations of the vertical slices through the model space presented in Figure 8B are shown with red lines.

Table A1
Acronyms Used in This Article

Acronyms	Name	Acronyms	Name
AG	Ariel Graben	LSS	Land Seismic Stations
ALR	DDE field	MCS	Multi-channel seismic data
CSS	Continental Shelf and Slope	OBS	Ocean Bottom Seismometers
CT	Central Terrace	PSTM	Pre-stack Kirchhoff time migration

Table A1
Continued

Acronyms	Name	Acronyms	Name
DP	Dana Plateau	WAS	Wide-angle seismic
MCP	Mozambique coastal plain		
MozR	Mozambique Ridge		
NNV	North Natal Valley		

Data Availability Statement

The data of the PAMELA-MOZ3 (Moulin & Aslanian, 2016) and PAMELA-MOZ5 (Moulin & Evain, 2016) cruises are archived and referenced at SISMER and accessible on request at https://doi.org/10.17600/16009500 and https://doi.org/10.17600/16001600.

Acknowledgments
We thank the captain, crew, and MCS technical team of the R/V Pourquoi-Pas?. We also thank the OBS technical team who maintain and constantly improve our OBS pool, as well as the land stations deployment team from Mozambique and Portugal. We thank WesternGeco and INP for permitting publication of seismic line: Profile A (MBWG13-27). The authors acknowledge the fruitful and constructive comments by Anouk Beniest and another anonymous reviewer, which greatly improved the manuscript. The GMT (Wessel & Smith, 1998), Seismic Unix (Cohen & Stockwell, 2019; Stockwell, 1999), and Geocluster (CGG-Veritas) software packages were used extensively in the redaction of this study.The PAMELA (PAssive Margins Exploration Laboratories) project was initiated in the early 2010th by TOTAL and IFREMER in collaboration with French universities (Université de Bretagne Occidentale, Université Rennes 1, Université Pierre and Marie Curie), the CNRS and the IFPEN. The Pamela MOZ3-5 cruises were led by M. Moulin, D. Aslanian, and M. Evain from Ifremer, in collaboration with Total.

References

Baby, G. (2017). *Mouvements verticaux des marges passives d'Afrique australe depuis 130 Ma, étude couplée: Stratigraphie de bassin - Analyse des formes du relief* (PhD, p. 342). Rennes 1 University.

Baby, G., Guillocheau, F., Boulogne, C., Robin, C., & Dall'Asta, M. (2018). Uplift history of a transform continental margin revealed by the stratigraphic record: The case of the Agulhas transform margin along the Southern African Plateau. *Tectonophysics*, *731–732*, 104–130. https://doi.org/10.1016/j.tecto.2018.03.014

Ben-Avraham, Z., Hartnady, C. J. H., & Le Roex, A. P. (1995). Neotectonic activity on continental fragments in the southwest Indian Ocean: Agulhas Plateau and Mozambique Ridge. *Journal of Geophysical Research*, *100*(B4), 6199–6211. https://doi.org/10.1029/94jb02881

Berthod, C., & Bachèlery, P. (2019). Cenozoïc volcanism and geodynamic. *PAMELA seminar, November 21 2019*. CSTJF PAU.

Christensen, N. I., & Mooney, W. D. (1995). Seismic velocity structure and composition of the continental crust: A global view. *Journal of Geophysical Research*, *100*(B6), 9761–9788. https://doi.org/10.1029/95JB00259

Cohen, J. K., & Stockwell, J. W., Jr. (2003). *CWP/SU: Seismic Unix Release 37: An open source package for seismic research and processing*. Center for Wave Phenomena, Colorado School of Mines.

Cohen, J. K., & Stockwell, J. W., Jr. (2019). CWP/SU: Seismic UnxRelease No. 44: An open source software package for seismic research and processing.

Cox, K. G. (1992). Karoo igneous activity, and the early stages of the break-up of Gondwanaland. In B. C. Storey, T. Alabaster, & R. J. Pankhurst (Eds.), *Magmatism and the causes of continental break-up* (Vol. 68, pp. 137–148). Geological Society, London, Special Publications.

Darracott, B. W. (1974). On the crustal structure and evolution of southeastern Africa and the adjacent Indian Ocean. *Earth and Planetary Science Letters*, *24*(2), 282–290. https://doi.org/10.1016/0012-821X(74)90106-X

Dingle, R. V., & Scrutton, R. A. (1974). Continental breakup and the development of post-Paleozoic sedimentary basins around southern Africa. *Geological Society of America Bulletin*, *85*(9), 1467–1474. https://doi.org/10.1130/0016-7606(1974)85<1467:cbatdo>2.0.co;2

Dunay, R. E., Braham, W., Cooper, M. K. E., Lester, M., & Tremolada, F. (2018). Micropalaeontological dating of the basal Cretaceous section of DSDP Site 249, Leg 25, Mozambique Ridge: Implications for the timing of the southern Atlantic–Indian Ocean connection. *Journal of Micropalaeontology*, *37*(1), 305–316. https://doi.org/10.5194/jm-37-305-2018

Eagles, G., & König, M. (2008). A model of plate kinematics in Gondwana breakup. *Geophysical Journal International*, *173*(2), 703–717. https://doi.org/10.1111/j.1365-246x.2008.03753.x

Evain, M., Schnürle, P., Leprêtre, A., Verrier, F., Watremez, L., Dias, N. A., et al. (2021). Crustal structure of the East-African Limpopo margin, a strike-slip rifted corridor along the continental Mozambique Coastal Plain and North-Natal Valley. *Solid Earth*, *12*, 1865–1897. https://doi.org/10.5194/se-2020-209

Fischer, M. D., Uenzelmann-Neben, G., Jacques, G., & Werner, R. (2017). The Mozambique Ridge: A document of massive multistage magmatism. *Geophysical Journal International*, *208*(1), 449–467. https://doi.org/10.1093/gji/ggw403

Flores, G. (1964). On the age of the Lupata rocks, lower Zambezi River, Mozambique. *Transactions of the Geological Society of South Africa*, *67*, 111–118.

Flores, G. (1973). The Cretaceous and Tertiary basins of Mozambique and Zululand. In *Association of African Geological Surveys in Symposium of East African Coastal Basins Paris*.

Georgen, J. E. (2008). Mantle flow and melting beneath oceanic ridge–ridge–ridge triple junctions. *Earth and Planetary Science Letters*, *270*(3–4), 231–240. https://doi.org/10.1016/j.epsl.2008.03.040

Gohl, K., & Uenzelmann-Neben, G. (2001). The crustal role of the Agulhas Plateau, southwest Indian Ocean: Evidence from seismic profiling. *Geophysical Journal International*, *144*(3), 632–646. https://doi.org/10.1046/j.1365-246x.2001.01368.x

Gohl, K., Uenzelmann-Neben, G., & Grobys, N. (2011). Growth and dispersal of a Southeast African large igneous province. *South African Journal of Geology*, *114*(3–4), 379–386. https://doi.org/10.2113/gssajg.114.3-4.379

Guillocheau, F. (2019). Post-rift evolution: Stratigraphy, paleogeography, climate, deformation. In *PAMELA seminar, November 21 2019*. CSTJF PAU.

Guillocheau, F., & Liget, A. (2009). *Bases de données paléogéographiques en Afrique permien terminal jurassique inférieur etude des bassins "karoo"*. Géociences-Rennes Université de Rennes 1/CNRS (UMR 6118).

Hanyu, T., Nogi, Y., & Fujii, F. (2017). Crustal formation and evolution processes in the Natal Valley and Mozambique Ridge, off South Africa. *Polar Science*, *13*, 66–81. https://doi.org/10.1016/j.polar.2017.06.002

Hartnady, C. J. H., Ben-Avraham, Z., & Rogers, J. (1992). Deep-ocean basins and submarine rises off the continental-margin of south-eastern Africa: New geological research. *South African Journal of Science*, *88*, 534–539.

Jacques, G., Hauff, F., Hoernle, K., Werner, R., Uenzelmann-Neben, G., Garbe-Schönberg, D., & Fischer, M. (2019). Nature and origin of the Mozambique Ridge, SW Indian Ocean. In *Chemical Geology* (Vol. 507, pp. 9–22). https://doi.org/10.1016/j.chemgeo.2018.12.027

Jourdan, F., Féraud, G., Bertrand, H., Kampunzu, A. B., Tshoso, G., Watkeys, M. K., & Le Gall, B. (2005). Karoo large igneous province; brevity, origin, and relation to mass extinction questioned by new $^{40}Ar/^{39}Ar$ age data. *Geology*, *33*(9), 745–748. https://doi.org/10.1130/g21632.1

König, M., & Jokat, W. (2010). Advanced insights into magmatism and volcanism of the Mozambique Ridge and Mozambique Basin in the view of new potential field data. *Geophysical Journal International*, *180*(1), 158–180. https://doi.org/10.1111/j.1365-246X.2009.04433.x

Lafourcade, P. (1984). *Etude géologique et géophysique de la marge continentale au Sud de Mozambique (17°S à 28°S)* (PhD dissertation). Université Pierre & Marie Curie.

Leinweber, V. T., & Jokat, W. (2011). Is there continental crust underneath the Northern Natal Valley and the Mozambique Coastal Plains? *Geophysical Research Letters*, *38*(14), L14303. https://doi.org/10.1029/2011gl047659

Leprêtre, A., Schnürle, P., Evain, M., Verrier, F., Moorcroft, D., de Clarens, P., et al. (2021). Deep structure of the North Natal Valley, from the Mozambique Coastal Plain to the Naude Ridge, using combined wide-angle and reflection seismic data. *Journal of Geophysical Research*, *126*(4), e2020JB021171. https://doi.org/10.1029/2020JB021171

Liu, Z., & Bleistein, N. (1995). Migration velocity analysis: Theory and an iterative algorithm. *Geophysics*, *60*(1), 142–153. https://doi.org/10.1190/1.1443741

Loureiro, A., Afilhado, A., Matias, L., Moulin, M., & Aslanian, D. (2016). Monte Carlo approach to assess the uncertainty of wide-angle layered models: Application to the Santos Basin, Brazil. *Tectonophysics*, *683*, 286–307. https://doi.org/10.1016/j.tecto.2016.05.040

Lutter, W. J., & Nowack, R. L. (1990). Inversion for crustal structure using reflections of the PASSCAL Ouachita experiment. *Geophysical Journal International*, *95*(B4), 4633–4646. https://doi.org/10.1029/jb095ib04p04633

Martin, A. K., Hartnady, C. J. H., & Goodlad, S. W. (1981). A revised fit of South America and South Central Africa. *Earth and Planetary Science Letters*, *54*, 295–305. https://doi.org/10.1016/0012-821X(81)90012-1

Mougenot, D., Gennesseaux, M., Hernandez, J., Lepvrier, C., Malod, J. A., Raillard, S., et al. (1991). The Mozambique Ridge (Indian Ocean)—A continental fragment shaped during the transform motion of American and Antarctic plates along East Africa. *Comptes Rendus de l'Académie des Sciences-Série II*, *312*, 655–662.

Moulin, M., & Aslanian, D. (2016). PAMELA-MOZ03 cruise, RV Pourquoi pas? https://doi.org/10.17600/16001600

Moulin, M., Aslanian, D., Evain, M., Leprêtre, A., Schnurle, P., Verrier, F., et al. (2020). Gondwana breakup and passive margin genesis: Messages from the North Natal Valley. *Terra Nova*, *32*(3), 205–214. https://doi.org/10.1111/ter.12448

Moulin, M., & Evain, M. (2016). PAMELA-MOZ05 cruise. https://doi.org/10.17600/16009500

Mueller, C. O., & Jokat, W. (2019). The initial Gondwana break-up: A synthesis based on new potential field data of the Africa-Antarctica Corridor. *Tectonophysics*, *750*, 301–328. https://doi.org/10.1016/j.tecto.2018.11.008

Nguyen, L. C., Hall, S. A., Bird, D. E., & Ball, P. J. (2016). Reconstruction of the East Africa and Antarctica continental margins. *Journal of Geophysical Research: Solid Earth*, *121*(6), 4156–4179. https://doi.org/10.1002/2015JB012776

O'Connor, J. M., Jokat, W., Regelous, M., Kuiper, K. F., Miggins, D. P., & Koppers, A. A. P. (2019). Superplume mantle tracked isotopically the length of Africa from the Indian Ocean to the Red Sea. *Nature Communications*, *10*(1), 5493. https://doi.org/10.1038/s41467-019-13181-7

Ponte, J. P. (2018). *Le système sédimentaire Zambèze, enregistrement du mouvement vertical de la marge Mozambicaine du Crétacé à l'actuel* (Vol. 1, p. 150). Thèse de l'Université de Rennes.

Ponte, J. P., Robin, C., Guillocheau, F., Popescu, S., Suc, J. P., Dall'Asta, M., et al. (2019). The Zambezi delta (Mozambique channel, East Africa): High resolution dating combining bio- orbital and seismic stratigraphies to determine climate (palaeoprecipitation) and tectonic controls on a passive margin. *Marine and Petroleum Geology*, *105*, 293–312. https://doi.org/10.1016/j.marpetgeo.2018.07.017

Raillard, S. (1990). *Les marges de l'Afrique de l'Est et les zones de fracture associées; Chaine Davie et Ride du Mozambique* (Ph.D. thesis) (pp. 1–200). Laboratoire de Géodynamique sous-marine Villefranche-sur-mer et Département de Géologie Océanique Paris, Université Pierre et Marie Curie.

Reeves, C., Teasdale, J. P., & Mahanjane, E. S. (2016). Insight into the Eastern Margin of Africa from a new tectonic model of the Indian Ocean. In M. Nemcok, S. Rybar, S. T. Sinha, S. A. Hermeston, & L. Ledvényiova (Eds.), *Transform Margins; Development, Controls and Petroleum Systems* (p. 431). Geological Society, London, Special Publications. https://doi.org/10.1144/SP431.12

Revillon, S. (2019). Magma genesis and the formation of the Mozambique margin: Inputs from geochemistry. In *PAMELA seminar, November 21 2019*. CSTJF PAU.

Sahabi, M. (1993). *Modèle général de l'évolution de l'océan Indien* (Thèse de doctorat) (Vol. 1–2, pp. 187–243).Université de Bretagne Occidentale.

Said, A., Moder, C., Clark, S., & Ghorbal, B. (2015). Cretaceous–Cenozoic sedimentary budgets of the Southern Mozambique Basin: Implications for uplift history of the South African Plateau. *Journal of African Earth Sciences*, *109*, 1–10. https://doi.org/10.1016/j.jafrearsci.2015.05.007

Salman, G., & Abdula, I. (1995). Development of the Mozambique and Rovuma sedimentary basins, offshore Mozambique. *Sedimentary Geology*, *96*(1–2), 7–41. https://doi.org/10.1016/0037-0738

Sandwell, D. T., & Smith, W. H. F. (2009). Global marine gravity from retracked Geosat and ERS-1 altimetry: Ridge segmentation versus spreading rate. *Journal of Geophysical Research*, *114*(B1), B01411. https://doi.org/10.1029/2008JB006008

Schneider, W. A., & Backus, M. (1964). Ocean-bottom seismic measurements off the California coast. *Journal of Geophysical Research*, *69*(6), 1135–1143. https://doi.org/10.1029/jz069i006p01135

Scrutton, R. A. (1973). Structure and evolution of the sea floor south of South Africa. *Earth and Planetary Science Letters*, *19*(2), 250–256. https://doi.org/10.1016/0012-821X(73)90125-8

Shellnutt, J. G., Yeh, M. W., Suga, K., Lee, T. Y., Lee, H., & Lin, T. (2017). Temporal and structural evolution of the Early Paleogene rocks of the Seychelles microcontinent. *Scientific Reports*, *7*(1), 179. https://doi.org/10.1038/s41598-017-00248-y

Stockwell, J. W., Jr. (1999). The CWP/SU: Seismic Unix package. *Computers & Geosciences*, *25*(4), 415–419. https://doi.org/10.1016/S0098-3004(98)00145-9

Svensen, H., Corfu, F., Polteau, S., Hammer, Ø., & Planke, S. (2012). Rapid magma emplacement in the Karoo Large Igneous Province. *Earth and Planetary Science Letters*, *325–326*, 1–9. https://doi.org/10.1016/j.epsl.2012.01.015

Thompson, J. O., Moulin, M., Aslanian, D., Guillocheau, F., & de Clarens, P. (2019). New starting point for the Indian Ocean: Second phase of breakup for the Gondwana. *Earth-Science Reviews*, *191*, 26–56. https://doi.org/10.1016/j.earscirev.2019.01.018

Tikku, A. A., Marks, K. M., & Kovacs, L. C. (2002). An Early Cretaceous extinct spreading center in the northern Natal Valley. *Tectonophysics*, *347*(1–3), 87–108. https://doi.org/10.1016/s0040-1951(01)00239-6

Watkeys, M. K. (2002). Development of the Lebombo rifted volcanic margin of southeast Africa. In M. A. Menzies, S. L. Klemperer, C. J. Ebinger, & J. Baker (Eds.), *Volcanic rifted margins* (pp. 27–46). Geological Society of America, Special Paper.

Watremetz, L., Leroy, S., d'Acremont, E., Roche, V., Leprêtre, A., Verrier, F., et al. (2021). The Limpopo magmatic transform margin (South Mozambique) – Part 1: Insights from deep-structure seismic imaging. *Tectonics*, *40*, e2021TC006915. https://doi.org/10.1029/2021TC006915

Wessel, P., & Smith, W. H. F. (1998). New, improved version of Generic Mapping Tools released. *Eos, Transactions American Geophysical Union*, *79*(47), 579. https://doi.org/10.1029/98eo00426

White, R. S., McKenzie, D., & O'Nions, R. K. (1992). Oceanic crustal thickness from seismic measurements and rare earth element inversions. *Journal of Geophysical Research*, *97*(B13), 19683–19715. https://doi.org/10.1029/92JB01749

Zelt, C. A. (1999). Modelling strategies and model assessment for wide-angle seismic traveltime data. *Geophysical Journal International*, *139*(1), 183–204. https://doi.org/10.1046/j.1365-246x.1999.00934.x

Zelt, C. A., & Barton, P. J. (1998). Three-dimensional seismic refraction tomography: A comparison of two methods applied to data from the Faeroe Basin. *Journal of Geophysical Research*, *103*(B4), 7187–7210. https://doi.org/10.1029/97jb03536

Zelt, C. A., & Forsyth, D. A. (1994). Modeling wide-angle seismic data for crustal structure: Southeastern Grenville Province. *Journal of Geophysical Research*, *99*(B6), 11687–11704. https://doi.org/10.1029/93JB02764

Zelt, C. A., & Smith, R. B. (1992). Seismic travel time inversion for 2-D crustal velocity structure. *Geophysical Journal International*, *108*(1), 16–34. https://doi.org/10.1111/j.1365-246x.1992.tb00836.x